On the microstructure and texture of intermetallics in Al/Mg/Al multi-layer composite fabricated by Accumulative Roll Bonding

Ismail Bencherifa, Baya Alili, Thierry Baudin, François Brisset, Dominique Thiaudière, Cristian Mocuta, Djamal Bradai

To cite this version:

Ismail Bencherifa, Baya Alili, Thierry Baudin, François Brisset, Dominique Thiaudière, et al.. On the microstructure and texture of intermetallics in Al/Mg/Al multi-layer composite fabricated by Accumulative Roll Bonding. Micron, 2023, 173, pp.103507. 10.1016/j.micron.2023.103507 . hal-04245368

HAL Id: hal-04245368
https://hal.science/hal-04245368

Submitted on 17 Oct 2023

On the microstructure and texture of intermetallics in Al/Mg/Al multi-layer composite fabricated by Accumulative Roll Bonding

Ismail Bencherifa [a,*], Baya Alili [b], Thierry Baudin [c], François Brisset [c], Dominique Thiaudière [d], Cristian Mocuta [d], Djamal Bradai [b]

[a] Laboratory of Metallic and Semiconducting Materials (LMSM), Department of Mechanical Engineering, University of Biskra, B.P.145, 07000, Biskra, Algeria.

[b] Laboratory of Materials Physics, Faculty of Physics, University of Sciences and Technology, Houari Boumediene (U.S.T.H.B.), P.O. Box 32, El-Alia, Bab-Ezzouar, DZ- 16111, Algiers, Algeria.

[c] Université Paris-Saclay, CNRS, Institut de chimie moléculaire et des matériaux d'Orsay, 91405 Orsay, France

[d] Synchrotron SOLEIL, Saint-Aubin, 91192 Gif-sur-Yvette, France.

* Corresponding author: Ismail BENCHERIFA, email: smail.bencherifa@univ-biskra.dz

Abstract

The microstructure and texture of the intermetallics in Al/Mg/Al multi-layer composite fabricated by Accumulative Roll Bonding (ARB) at 400 °C up to 6 cycles were investigated using Electron BackScatter Diffraction (EBSD) and Synchrotron X-ray Diffraction (SXRD). EBSD and SXRD analysis have shown that ARB processing leads to the formation of Al_3Mg_2 and $Mg_{17}Al_{12}$ intermetallics soon after the second ARB cycle with a global thickness of 12 (N=2) to 22 µm (N=6). The polycrystalline intermetallics plates growth was columnar and normal to the bonding interface. A constitutional liquefaction region was depicted ahead of the plates with an unusual rugged migration front. The Al_3Mg_2 and $Mg_{17}Al_{12}$ intermetallic compounds which formed after 2 ARB cycles have approximately the same average grain size (1.0 µm) at this cycle. After

4 ARB cycles, the grain refinement of Al_3Mg_2 is more than 4 times higher than in $Mg_{17}Al_{12}$. The average grain size of Al_3Mg_2 and $Mg_{17}Al_{12}$ reach 0.2 and 0.9 µm, respectively. After 6 cycles of ARB, the average grain size of both Al_3Mg_2 and $Mg_{17}Al_{12}$ increased to 1.5 µm and 2.8 µm, respectively. The dislocation density obeyed a $\rho_{Al3Mg2} > \rho_{AZ31} > \rho_{Al\ 1050} \sim \rho_{Mg17Al12}$ hierarchy after N=4 and 6 ARB cycles and the Al_3Mg_2 was shown to store more dislocations.

Through the ARB processing, a usual strong basal (0002) texture was depicted in AZ31 layers and a weak rolling texture was shown in Al 1050 layers with a dominant Rotated Cube (001) <110> component that vanished after upon increasing ARB cycles. The Al_3Mg_2 and $Mg_{17}Al_{12}$ intermetallics were characterized by a random texture.

Keywords: Al1050/AZ31/Al1050; Accumulative roll bonding; Microstructure; Texture; Intermetallic compounds; Dislocation density.

1. Introduction

The fabrication of hybrid metal composite containing different components has been an effective way to enhance mechanical properties, i.e., plasticity, stiffness, interlaminar strength, abrasion resistance, impact performance, etc. (Nie et al., 2019). A metallic multi-layer composite sheet is a typical hybrid metal composite (Boon and Joshi, 2020). Over the past few years, regarding the materials science community, there has been a significant surge of interest in the use of metallic multi-layer composite sheets for structural applications largely due to their exceptional properties. This has led to a successful fabrication of a diverse range of multi-layer composite sheets, including Ti/Al (Li et al., 2022; Wang et al., 2020), Ni/Ti (Mokhles et al., 2020), Al/Cu (Lee and Jeong, 2023), Al/Steel (Verstraete et al., 2019), and Mg/Al (Habila et al., 2019; Nie et al., 2018). Specifically, Al- and Mg-based alloys, owning to their lower density, are greatly used as lightweight materials across a range of fields, notably in automotive, aerospace, and biomaterials applications.(Habila et al., 2019; Kumar et al., 2020). Therefore, they have suitable metallurgical compatibility as well as close melting and recrystallization temperatures (Song et al., 2022).

Very interestingly, recently, Ruizhi Wu's team (Zhang et al., 2023b)(Zhang et al., 2023a)(Xie et al., 2023b)(Xie et al., 2023b) have developed a dilute Mg-RE alloy (Mg-0.3at%Er) with ultrahigh ductility (near 50%) at RT by minor Er alloying and moderate grain refinement (Zhang et al., 2023b) . Trace Er addition have simultaneously improved the mechanical and anti-corrosion properties of extruded Mg-Al (Zhang et al., 2023a) . They have proposed an effective way to develop high-strength corrosion resistant Mg alloys by controlling the potential fluctuation to form a "uniform potential" strengthening microstructure in Mg-14.4Er-1.44Zn-0.3Zr (wt.%) alloys containing hybrid structures, i.e., elongated long-period stacking ordered (LPSO) blocks +

intragranular stacking faults (SFs)/LPSO lamellae (Xie et al., 2023b). Furthermore, they succeed to design Mg96.9Y1.2Ho1.2Zn0.6Zr0.1 (at.%) alloy with high mechanical and anti-corrosion properties by constructing "homogeneous potential strengthening microstructure", such as the weak anode nano-lamellar SESFs structure (Xie et al., 2023a).

The development of a Mg/Al laminated composite has been expected as a promising approach to integrate the desirable characteristics of dissimilar metals within a single composite material. Al and its alloys have long been recognized for their exceptional formability and resistance to corrosion, making them an ideal candidate for such an application.(Mo et al., 2022; Raei et al., 2010). In contrast, Mg and its alloys with a density of one-fourth of steel have an excellent damping capacity, recyclability, high specific stiffness, and strength (Lee et al., 2022; Li et al., 2015). Rahmatabadi et al. (Rahmatabadi et al., 2018) report that the ultimate tensile strength of the Al/Cu/Mg laminated composite fabricated via the Accumulative Roll Bonding (ARB) processing was close to 355.5 MPa. This value was about 3.2, 2 and 2.1 times higher than the nominal values corresponding to magnesium, copper, and aluminum, respectively. Actually, due to big differences in physical/chemical properties and crystal structures, the joining of Al alloy to Mg alloy keeps facing great challenges. Unfortunately, it is very difficult to apply fusion processing for joining Al to Mg alloy sheets. The formation of intermetallic compounds (IMCs) will cause embrittlement of the welds due to the high rates of diffusivity in the liquid phase (Panteli et al., 2012). However, besides the ARB processing, some other techniques have been employed to develop the Mg/Al laminated composite such as friction stir welding (FSW) (Beygi et al., 2021), explosive welding (Acarer et al., 2022) and compound casting (Guan et al., 2022). Among them, the ARB processing, as Severe Plastic Deformation (SPD) technique, is one of the most popular technique candidate for industrial applications. Its common advantages and features are high production efficiency, high product quality, stability, simple processing, and easy mass production (Rahmatabadi et al., 2018). Furthermore, ARB processing is considered as a solid-state bonding technique. Solid-state bonding consists mainly of two kinds: mechanical and diffusion (Kim et al., 2015). The quality of metallurgical bonding is determined by diffusion bonding (Guo et al., 2019). Thus, during the ARB processing of two or more dissimilar metals, the diffusion layer structure is dependent on the inter-diffusion of atoms species and the formation of IMCs at the interfaces. According to the Al-Mg phase diagram, different IMCs can form at the Al/Mg interface such as $Mg_{17}Al_{12}$ and Al_3Mg_2 and the structure and the composition of the diffusion layer have been widely studied in Mg/Al laminated composite fabricated by various processing (Acarer et al., 2022; Beygi et al., 2021). To date, other possible IMCs present in the Mg-Al system (e.g. R or ε, and λ phases) have not been evidenced in welding studies (Panteli et al., 2012). When the IMCs have formed a continuous layer at the Mg/Al interface, the subsequent growth is only possible by diffusion through the IMC itself and an abrupt change in kinetics is often observed (Wang et al., 2015). Usually, the IMCs have different properties compared to the parent metals. Therefore, the microstructures of both parent metals and IMCs formed at the Mg/Al interface have a significant effect on the bonding strength and mechanical properties of the laminated composite. Wherefore, the control of the IMC layer formation is critical to assure interface properties. Recently, in Al/Mg/Al laminated composite produced by ARB processing, Habila et al. (Habila et al., 2019) reported that the decrease in the yield and ultimate strengths after 3 ARB cycles, is due mainly to the failure and crack of IMCs which appeared after the fourth cycle. Unfortunately, experimental studies on the metallurgical behavior of the development of IMCs cannot explain the physical mechanism behind this phenomenon, because their formation and kinetic characteristic are immensely complex to be quantified. Therefore, several studies have developed models that predict growth kinetics of the intermetallic phases (IMCs) formed in a reactive diffusion couple between two metals (Song et al., 2022; Wang et al., 2015). Dislocation behavior during severe plastic deformation in laminated composites plays a crucial role in ductility and strength of bulk materials. Therefore, for more understanding the microstructure of laminated composite, it is important to use different characterization methods in order to quantitatively evaluate the dislocation density and the hardening behavior of each layer in IMCs under deformation (Jiang et al., 2022). Technically, it is important to note that it is difficult to estimate the dislocation density and its evolution near the interface in laminated composite by conventional approaches such as transmission electron microscopy (TEM) and/or conventional XRD owing to the inhomogeneous nature of dislocation slips (Bay et al., 1992). However, in recent years, significant progress in the development of new experimental characterization techniques has provided promising opportunities such as Electron BackScatter Diffraction (EBSD) and Synchrotron X-ray Diffraction (SXRD). Analysis of EBSD orientation maps provide information on dislocations at a mesoscopic scale by averaging many discrete orientation data collection. SXRD measured patterns are by default averaged over many grains and thus directly convey microstructure-averaged (bulk) information. SXRD available at a synchrotron radiation source has been established as a powerful technique for in-deep studies of structure and phase transformation kinetics in different materials (Malinov et al., 2002). Furthermore, the Line Profile Analysis (LPA) of diffraction patterns is an indirect powerful method to obtain various microstructural parameters in crystalline materials (Muránsky et al., 2019).

In the author’s opinion, a close review of the existing literature does suggest a lack of knowledge about the texture and microstructure of IMCs in Al 1050/AZ31/Al 1050 laminated composite produced by ARB.

In this framework, the present study aimed at investigating the microstructural, dislocations density evolution as well as the textural properties of the different phases formed at the interface of an Al 1050/AZ31/Al 1050 laminated composite fabricated via the ARB processing for up to 6 cycles using EBSD and SXRD techniques.

2. Experimental Techniques

Commercially pure Al1050 and AZ31 alloys were used in this study. The nominal chemical compositions of the materials are shown in Table 1 and Table 2, respectively. The initial Al 1050 sheets with average grains size of around 25 μm and 1 mm of thickness were supplied by PIMA (Produits Industriels et Métallurgiques SARL, Algeria) Company, Algeria. The initial AZ31 sheets with average grains size of around 18 μm and 2.0 mm of thickness were supplied by MagIC Magnesium Innovations Center, Germany. The ARB processing principle is shown in Fig. 1. The as-received Al 1050 and AZ31 foils were cut into sheets with dimensions of 65 mm × 30 mm. The initial sheets were cleaned and degreased in acetone, then wire brushed to remove the surface oxide film and create a certain roughness in order to insure good bonding. The prepared initial sheets were stacked in the following order Al 1050/AZ31/Al 1050. To avoid any lateral slipping during rolling, the stacks were tightly tied with a soft steel wire. The stacks were annealed at 400 °C for 10 min in a preheated furnace to enhance their mechanical workability during the ARB processing. Subsequently, the stacks were hot-roll bonded with a thickness reduction of 50% during each cycle without lubrication. The sheets were air-cooled and then cut into equal long sheets in order to proceed the second cycle. Thereafter, the ARB processing was repeated for up to 6 cycles and the rolling direction was kept constant throughout the ARB processing. Hence, regarding the von Mises equivalent strain (E et al., 2016), the calculated strain value is 0.8 for the Al 1050/AZ31/Al 1050 laminated composite in each ARB cycle.

The microstructure observations and texture analysis of the Al1050/AZ31/Al1050 laminated composite were carried out by EBSD measurements on the longitudinal cross-section (RD-ND plane, see Fig. 1). Standard metallographic preparation (mechanical polishing using SiC papers up to grid 4000, then diamond suspension down to 1/4 of a micron was used and finished by ionic polishing. Samples were positioned in a Gatan PECS II system using the planar mode for the cross-sectional EBSD acquisitions. The EBSD measurements were carried out using a TSL-EDAX-Hikari system mounted on a scanning electron microscope FEG-SEM ZEISS Supra 55 VP operating at 20 kV. The data acquisition and analysis were processed by the Orientation Imaging Microscopy, OIM™ software. A grain dilation and grain Confidence Index (CI) standardization clean-up-with a grain tolerance angle of 5° and a minimum grain size of 5 pixels were applied to improve the quality of EBSD raw data. The scanned area and the step size in the RD-ND plane, were 60×30 μm^2 and 0.1 µm, 65 × 65 μm^2 and 0.1 µm, 50×25 μm^2 and 40 nm for N=2, 4 and 6 ARB processed samples, respectively. In the EBSD maps, boundaries with more than 15° misorientations were defined as High-Angle Grain Boundaries (HAGBs) and those with 2°-15° misorientations as Low-Angle Grain Boundaries (LAGBs). The calculation of the crystallographic texture from EBSD measurements was performed using OIM^{TM} software. The Orientation Distribution Functions (ODFs) were assessed using the harmonic method (L = 22), and a Gaussian function with a half-width of 5°.

Kernel Average Misorientation (KAM) method in OIM™ software was used for the dislocation density assessment. KAM is known as the average misorientation angle of a given point with all its neighbors belonging to the same grain (Wang et al., 2022). In the present case, the θ_{KAM} value was calculated from the mean misorientation angle between a given point and its

3rd neighbors excluding misorientations of 5°. Hence the dislocation density can be obtained following Eq. (1) (Azzeddine et al., 2020):

$$\rho = \frac{\alpha\theta_{KAM}}{ndb} \dots\dots\dots\dots\dots\dots\dots\dots\dots (1)$$

Where $\alpha = 3$ is the average value between pure tilt ($\alpha = 2$) and pure twist ($\alpha = 4$) grain boundaries (Azzeddine et al., 2020), n is the nearest neighbor, d is the scan step size and b is the Burgers vector, 0.28 nm (Mo et al., 2022), 0.32 nm (Ren et al., 2022), 0.165 nm (Wen and Chen, 2014) and 0.32 nm (Vaid et al., 2019), for Al 1050, AZ31, Al_3Mg_2, and $Mg_{17}Al_{12}$, respectively.

The special features of synchrotron radiation and dedicated equipment (2D detectors), owing to strong material penetration by x-ray radiation, high photon fluxes, and high count rates, insure a non-destructive approach to probing a material very quickly. Indeed, it is very helpful in the case of phases such as Al_3Mg_2 and $Mg_{17}Al_{12}$ with small volume fractions.

The present phases were indexed using the ICSD database (Al, Cubic, Fm-3m, Ref: 98-004-3423, Mg, Hexagonal; F63/mmc, Ref: 98-005-2260, Al_3Mg_2, Cubic, Fd-3m, Ref: 98-005-7964) and $Mg_{17}Al_{12}$, Cubic, I-43m, Ref: 98-002-3607).

The SXRD measurements were carried out on the DIFFABS beamline, Synchrotron SOLEIL, France. A new 2D X-ray hybrid pixel detector (CirPAD) was used in order to record X-ray diffraction patterns in the [0-130°] 2θ range and in reflection mode. More information about the new detector CirPAD are available elsewhere (Desjardins et al., 2022). The CirPAD is a new member of the XPAD detectors family that is the largest XPAD-based detector to date. The energy of the monochromatic X-ray beam was 18 keV ($\lambda = 0.06888$ nm). A Python homemade code was used to convert the images of the detector, by their azimuthal integration to obtain diffractograms, i.e. the average intensity distribution I (2θ) of the Debye rings. The Powder Diffraction File PDF-

4+2018 from the ICDD (International Centre of Diffraction Data) was used to identify the sample phases. The Scherrer-Wilson equation (Basak et al., 2022) is the simplest method to measure the crystallite size by peak broadening analysis and was used in this study. The Full Width at Half Maximum (FWHM) value of the highest peak was used to determine the average crystallite size *D* by this technique by the Eq. (2).

$$D = \frac{K\lambda}{\beta cos\theta} \dots\dots\dots\dots (2)$$

For the lattice-strain, the relation of Stokes (Stokes and Wilson, 1944) and Wilson were used as given in Eq. (3).

$$\varepsilon = \frac{\beta}{4\tan\theta} \dots\dots\dots (3)$$

Where β is the broadening of the reflection due to small crystallite sizes, with β = (B-b) (Malinov et al., 2002). B and b are the FWHM of the considered ARB processed and the standard (LaB_6) samples. K is approximately 0.9 (0.89 for spherical, 0.94 for cubic crystallite). λ is the wavelength, and θ is the diffraction angle. The dislocation density can be calculated from *D* and *ε* using the following formulae (Kapoor et al., 2005):

$$\rho_D = \frac{3}{D^2} \ \ and\ \rho_\varepsilon = \frac{k\varepsilon^2}{Fb^2} \dots\dots. (4)$$

$$\rho = (\rho_D \times \rho_\varepsilon)^{1/2} \dots\dots\dots. (5)$$

Where, $k = 6\pi$, F = 1 (Kapoor et al., 2005), and *b* is the magnitude of the Burgers vector.

Table 1. Chemical composition of AZ31 alloy (Weight %).

AZ31						
Mg	Al	Zn	Mn	Ca	Si	Cu
Bal	2.5-3.5	0.6-1.4	0.2-1.0	0.04	0.1	0.01

Table 2. Chemical composition of Al 1050 alloy (Weight %).

Al 1050								
Al	Cu	Fe	Mg	Mn	Si	Ti	V	Zn
99.5	0.05	0.4	0.05	0.05	0.25	0.03	0.05	0.05

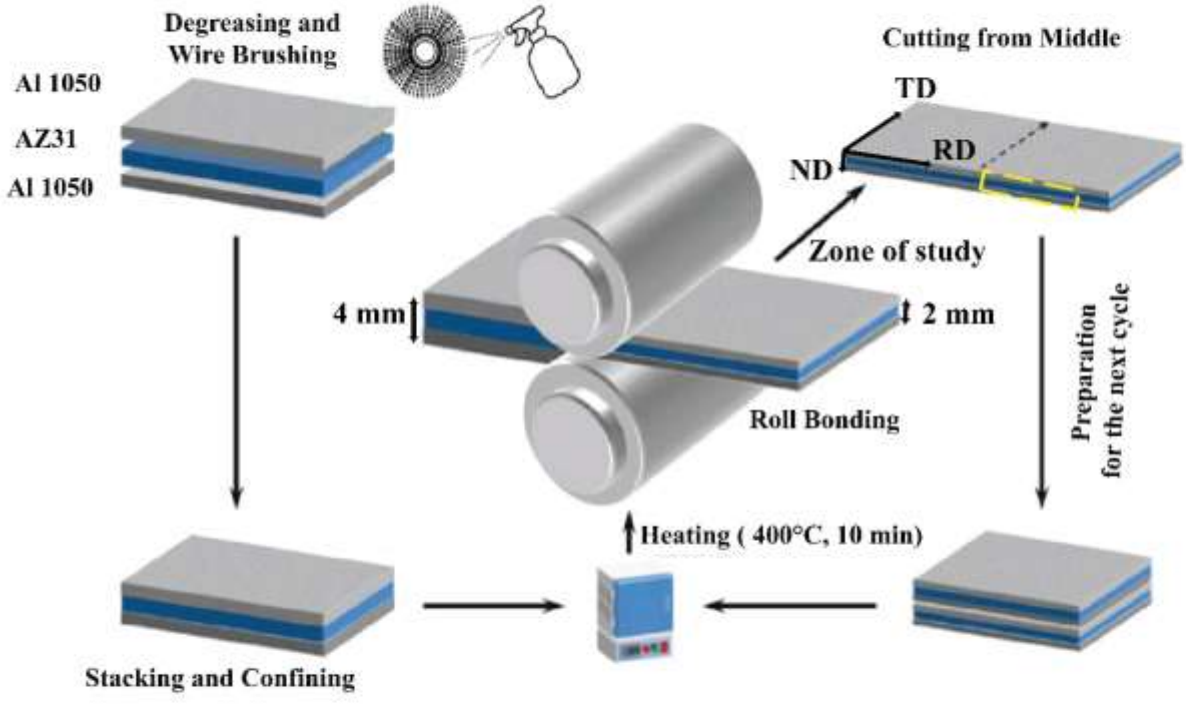

Fig. 1. Schematic illustration of the ARB processing.

3. Results and Discussion

3.1. Microstructure evolution of the parent AZ31, Al1050 alloys, and IMCs

Fig. 2(a–f) show the SEM cross-sectional images of Al 1050/AZ31/Al 1050 laminated composite after ARB processing for up to 6 cycles on the RD-ND plane in which the dark and light grey colors indicate the AZ31 layers and Al 1050 layers, respectively. The bonding quality between Al 1050 and AZ31 sheets is excellent after the 50% reduction of thickness with no observable imperfections such as cracks, pores, or de-lamination formed along the interfaces of Al1050/AZ31/Al1050 laminated composite after any ARB cycle. Also, it is difficult to distinguish between the Al 1050/Al 1050 interfaces introduced by each cycle which is the main indication of good bonding. As the ARB cycle increased, the thicknesses of both Al 1050 and AZ31 layers gradually decreased and were in the range of 0.1–0.15 mm after 6 ARB cycles **(**shown in Fig. 3**)**. However, from the third cycle, a rugged migration front of the layered structure was observed where the Mg layers started to locally neck and fracture (Fig. 2(c)). Essentially, the necking is found in the outer AZ31 layers of the composite and appears to be inclined at a 45° angle to the rolling direction (RD). The plastic behavior of AZ31 and Al 1050 materials is well-known to be very different. Therefore, during severe plastic deformation, the deformation inhomogeneities will be noticeably evident. Due to the varied flow characteristics of the constituent phases, plastic instabilities develop and subsequent deformation by ARB processing leads the AZ31 alloy layers to neck and eventually fragment. Moreover, upon increasing the number of ARB cycles, the AZ31 layer curvature becomes significant and more fractures did appear.

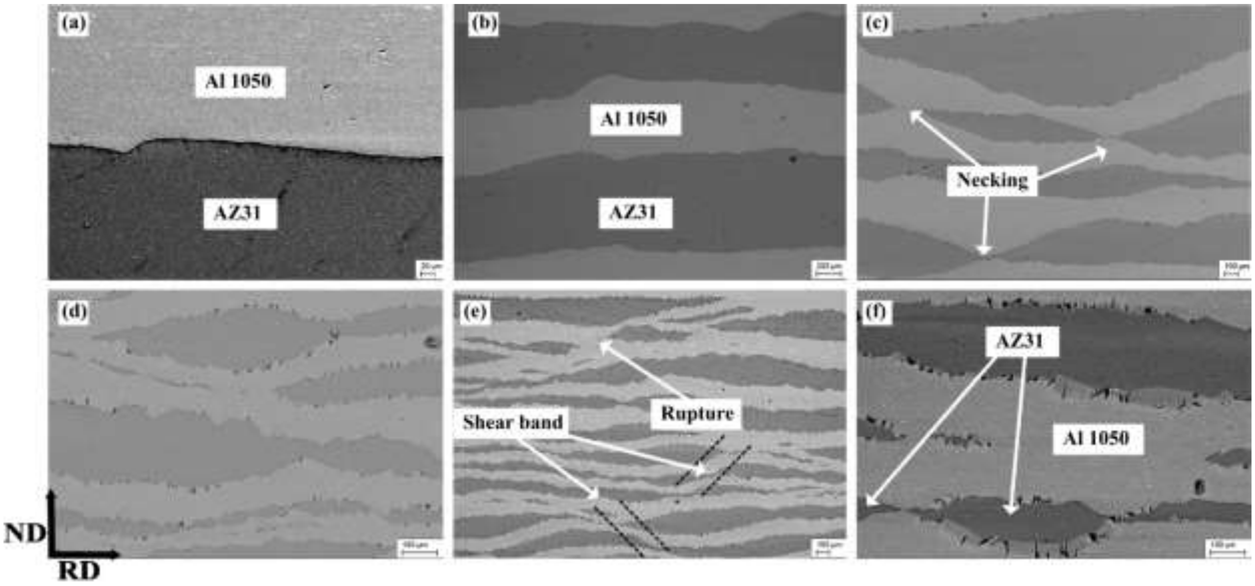

Fig. 2. SEM cross-sectional images of Al 1050/AZ31/Al 1050 laminated composite after ARB processing for at a) 1, b) 2, c)3, d) 4, e) 5, and f) 6 cycles on the RD-ND plane.

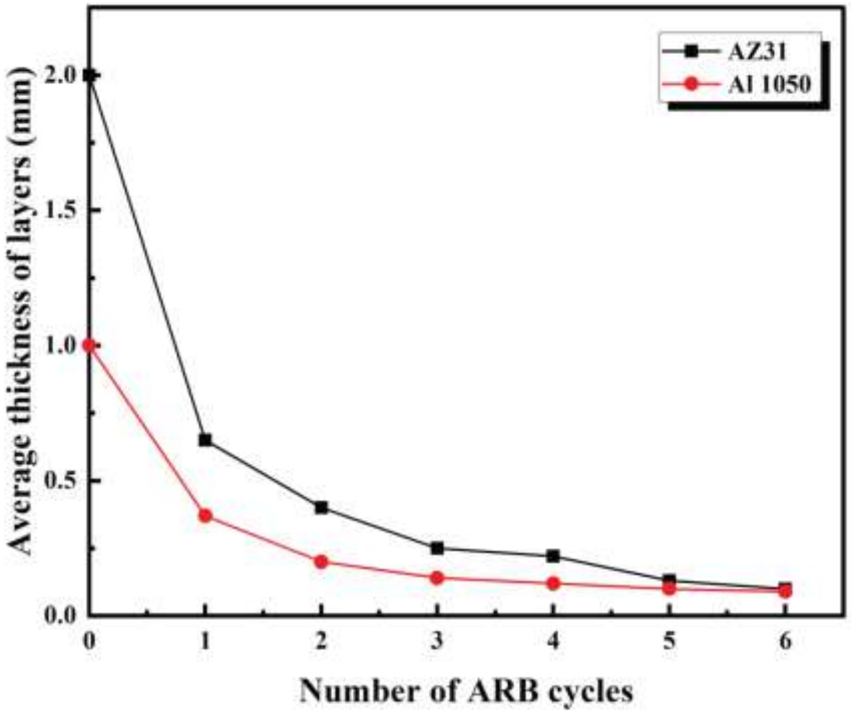

Fig. 3. Variation of the thickness of Al 1050 and AZ31 layers in Al 1050/AZ31/ Al 1050 multilayered composite during ARB cycles.

Fig. 2(c–f) show that the AZ31 sheets fragmented and are surrounded by Al 1050 ones because of large deformations and high temperatures.- Indeed, the longitudinal elongation leads the AZ31 sheet to bend and the Al 1050 sheet will fill the empty area. Similar results and phenomena were also reported in (Ohsaki et al., 2007; Yang et al., 2010) for Ti/Al and Cu/Ag laminated composite subjected to ARB processing.

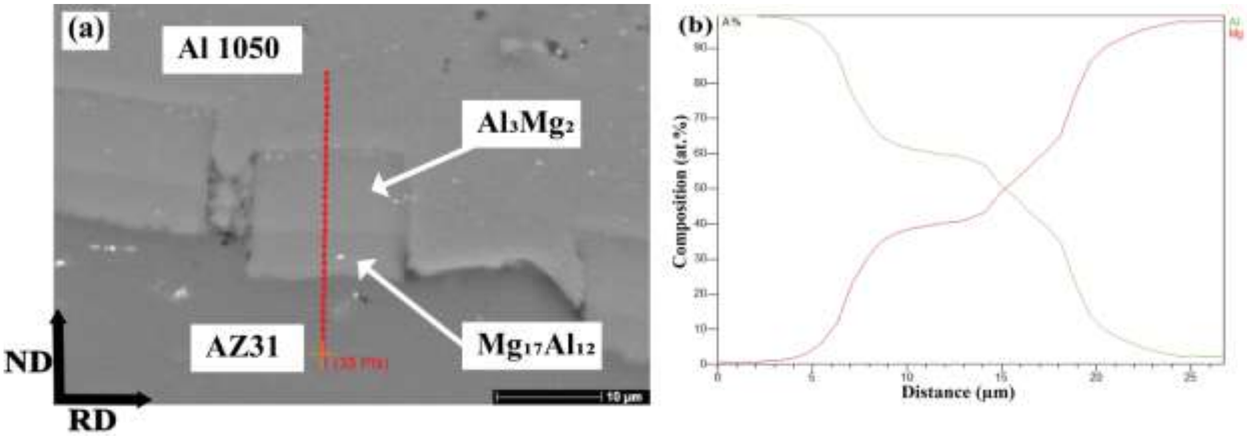

Fig. 4. EDS line-scanning analysis of the interface in the Al 1050 /AZ31/Al 1050 laminated composites after two cycles: (a) SEM image; (b) EDS line-scanning analysis of the interface

Fig. 4. shows the SEM micrographs of the Al 1050 /AZ31/Al 1050 bonding interface in the multilayered composite after 2 ARB cycles. One can depict that after one ARB cycle (Fig. 2(a)), the interfacial zone consists only of the Al 1050 layer beside the AZ31 layer, and no new intermetallic phases were observed in the bond interface. Meanwhile, after 2 ARB cycles, gray and light-shaded layers appeared beside AZ31 and Al 1050 sides, respectively (Fig. 2(b)). According to the composition analysis from EDS spectra and the binary Al-Mg binary alloy phase diagram (Chen et al., 2007), the new phases should be $Mg_{17}Al_{12}$ phase next to the AZ31 alloy and Al_3Mg_2 next to the Al 1050 alloy. Fig. 5 shows an elemental phase distribution map that clearly highlights the interface of different present phases after ARB processing up to N= 2, 4 and 6 cycles.

Additionally, the thickness of the $Mg_{17}Al_{12}$ phase is lower than the Al_3Mg_2 one (Fig.6), indicating that the diffusion of AZ31 atoms is lower than that of Al 1050 ones (Li et al., 2015). Song et al. (Song et al., 2022) stated that the different thickening kinetics of intermetallics compounds can be ascribed to variations in the composition, grain size, and substructure of the alloy substrate. Furthermore, it was observed that the type of the layers used can also influence the diffusion process According to data from the literature (Song et al., 2022), the $Mg_{17}Al_{12}$ phase is the first IMC phase to form but the Al_3Mg_2 phase has a faster growth rate. Hence, the $Mg_{17}Al_{12}$ phase nucleates first as a result of the Al matrix saturated with Mg solute earlier, and the nucleation occurred once a sufficient driving force (super-saturation) has been achieved. However, the $Mg_{17}Al_{12}$ phase has a higher activation energy for intracrystalline and grain boundary diffusion compared with the Al_3Mg_2 phase. The higher activation energy for diffusion in the $Mg_{17}Al_{12}$ phase makes interdiffusion arduous and therefore, the Al_3Mg_2 phase grows faster. In this study, the high strain level induced by ARB processing can increase the IMCs formation and speeds up the inter-diffusion between different layers of laminated composite. Similar results were reported by Hebert et al. (Hebert and Perepezko, 2004) and Zhang et al. (Zhang and Acoff, 2007). The diffusion zone can be affected by the Al atoms species in AZ31 layers, as well as the diffusion of Mg in Al 1050 layers and vice versa. Diffusion at the Al and Mg common interface results in more homogeneous connections in the subsequent cycles of the ARB procedure. This phenomenon is known as inter-diffusion resulting from deformation (Mansouri et al., 2019). Inter-diffusion may result from three mechanisms of atoms displacement through mechanical work, diffusion through dislocation pipes, and diffusion through blank locations created during severe plastic deformation (Mansouri et al., 2019).

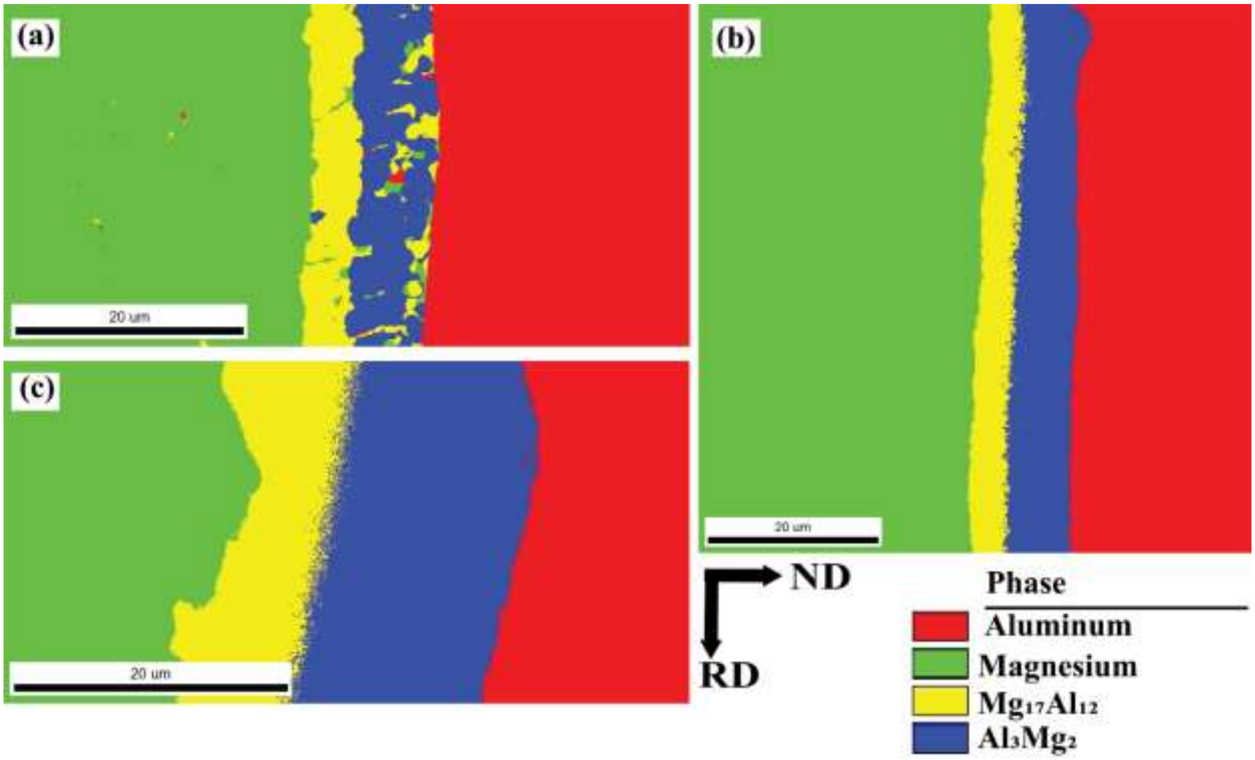

Fig.5 Elemental phase distribution map distinguish the interface of different phases after 2,4 and 6 ARB cycles.

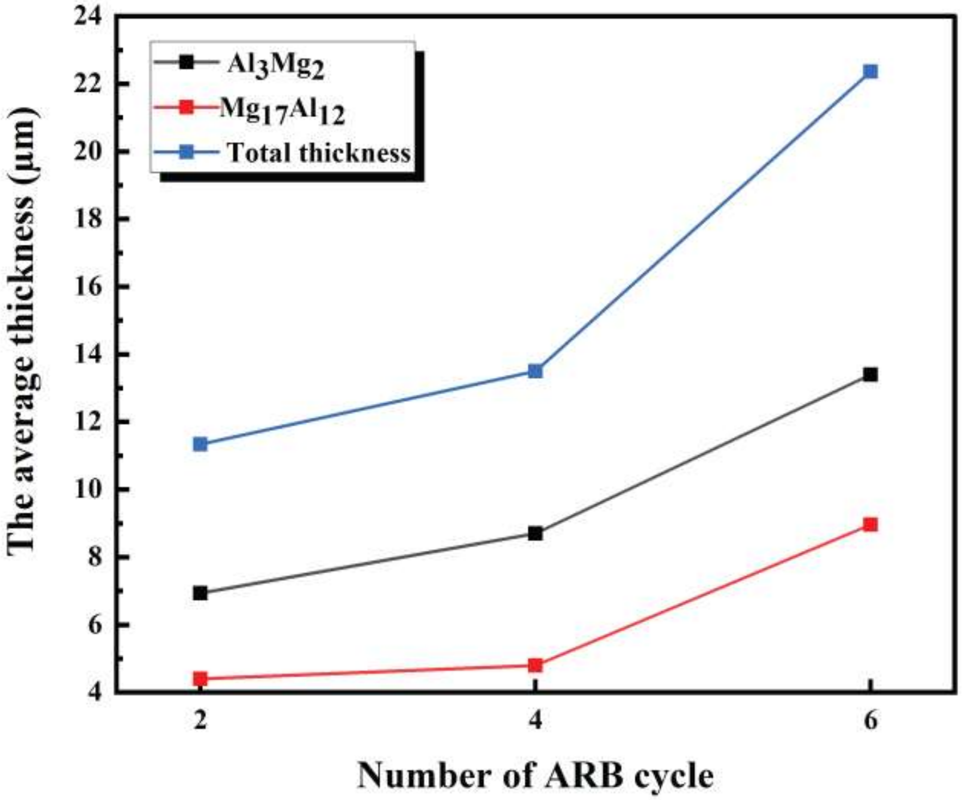

Fig.6 The average thickness of Al_3Mg_2 and $Mg_{17}Al_{12}$ intermetallic compounds after different ARB cycles.

The IMCs which previously appeared after two ARB cycles remained continuous in the (RD-ND) plane, then they cracked and broke up after three ARB cycles as shown in Fig. 7. The majority of cracks are in the normal direction (ND). Indeed, the cracks appeared from the Al_3Mg_2 phase and quickly propagate in the $Mg_{17}Al_{12}$ phase because of the brittleness of the IMCs (Nie et al., 2018). This may be ascribed to the difference in the brittleness and the stress level of the IMCs. Indeed, the Young modulus of the Al_3Mg_2 (E = 68.0 GPa) phase is higher than that of the $Mg_{17}Al_{12}$ (E = 60.7 GPa) intermetallic and hence is more brittle. However, in this study, no cracks or facture were observed in Al 1050 layer or AZ31 layer in all ARB cycles.

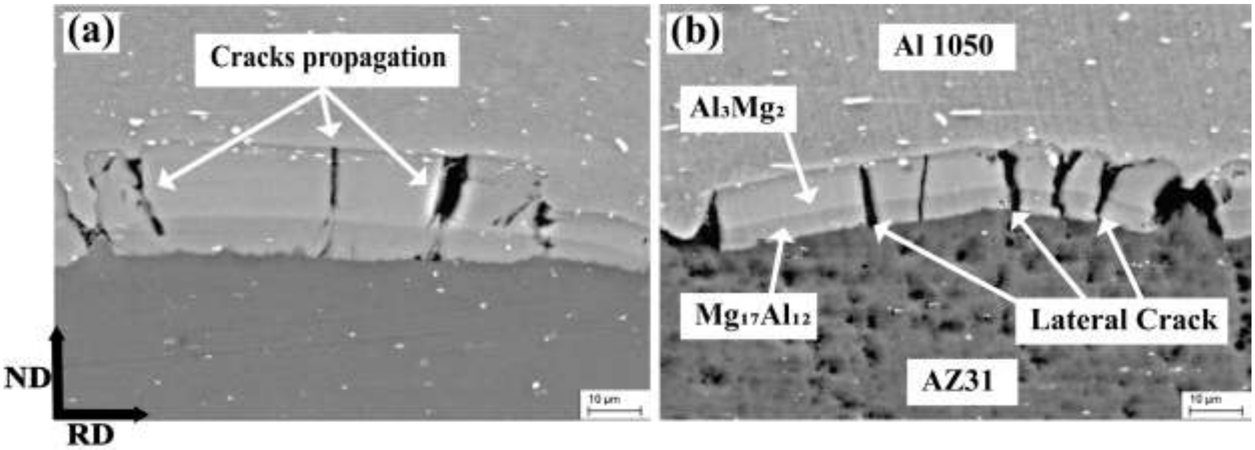

Fig. 7. SEM micrograph of Al 1050/AZ31/Al 1050 laminated composite after 4 ARB cycles. Cracks of intermetallics compounds are shown, as (a) discontinuous and (b) continuous cracks.

An unusual microstructural feature appeared after 6 cycles ARB on the side of $Mg_{17}Al_{12}$ with irregular shapes and did not appear near the Al_3Mg_2 interface as shown in Fig 8. (a). This irregular shape with an unstable and rugged migration front suggests that the phenomena of component liquefaction occurred during the ARB processing when the temperature in the interface reached or was above the eutectic temperature, therefore a liquid film was developed at the interface (Zhao et al., 2021). Fundamentally, a eutectic structure composed of $Mg_{17}Al_{12}$ (evidenced by the glitches (see arrows) in the linear EDS scan shown in Fig8. (b). The Mg solid solution was formed due to the partial melting of the Mg phase close to the interface. During the bonding of Al- and Mg-base plates, Al_3Mg_2 and $Al_{12}Mg_{17}$ intermetallic compounds may form as predictable from the phase diagram. Heating up above the eutectic line will cause the eutectic reactions $Mg + Al_{12}Mg_{17} \rightarrow L$ (at 437 ˚C) and $Al + Al_3Mg_2 \rightarrow L$ (at 450 ˚C), respectively. This liquid formation is called constitutional liquation (Sato et al., 2004). Both eutectic temperatures are about 200 ˚C below the melting points of Al and Mg elements, and they can be reached easily during SPD to form liquid films along the interface, and hence, lead to cracking (Gerlich et al., 2005). This is in line with the statement of Straumal et al. (Straumal et al., 2015) that the SPD treatment at ambient temperature T_{SPD} = 300 K is frequently equivalent to the heat treatment at a certain elevated temperature T_{eff} > 300 K called effective temperature (Straumal et al., 2015). Let's recall that in the present study, ARB processing was undertaken with a pre-heating at 400°C for 10 minutes. Under these latter conditions, the intermetallic formation is largely boosted. In fact, ARB processing is a solid-state joining processing, where a global melting of stacking materials does never occur. In the case of ARB laminated composite, nevertheless, it is possible that liquefaction may develop during the ARB processing. Furthermore, the strain rate (Haddadi, 2015; Panteli et al., 2012) reactions temperature (Yu et al., 2021) and local composition (Chen et al., 2018) are the metallurgical parameters that control the formation and growth of the intermetallic compounds. As it is known, the interaction between the sheet metals and the two rolls during the ARB processing leads to appreciable heat release. Similar phenomena was observed during the FSW processing because the interaction between the work-piece, tool and the pin rotation causes plastic deformation of the work-piece material. Beygi et al. (Beygi et al., 2021) reported that during friction stir welding (FSW) of Al/Mg the activity of the chemical species was reduced because of the liquefaction phenomenon and subsequent eutectic structures formation and as a result, the diffusion rate in the solid state was slowed down.

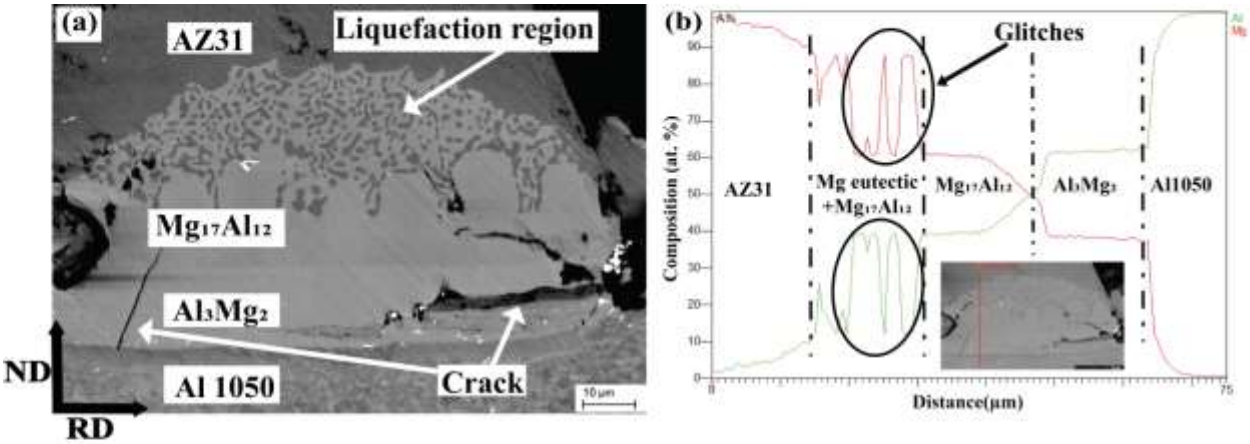

Fig. 8. Morphologies of the irregularly shaped region after 6 ARB cycles. (a) SEM micrograph, (b) linear EDS scans analysis across the line shown in the inset.

Fig. 9. shows the inverse pole figure (ND-IPF) maps (knowing that the texture was rotated to be described in the classical rolling coordinate system i.e. {hkl} // (RD-TD) and <uvw> // RD) of the Al 1050/AZ31/Al 1050 laminated composite after 2, 4, and 6 ARB cycles. It is worth noting, that, in the present study, contrary to some previous works, the Al_3Mg_2 and $Mg_{17}Al_{12}$ IMCs are observably indexed and resolved by the OIM™ technique. After 2 ARB cycles, the microstructure of the AZ31 layer consists of two different types of grains, large elongated grains along RD and small equiaxed ones distributed between the formers. No twins were observed and the average grain size of the AZ31 layer dramatically decreased from 18.1 (N = 0) down to 1.9 µm (N = 2) (Fig. (10)). After 4 ARB cycles, a homogeneous microstructure of the AZ31 layer with refined and equiaxed grains was obtained as shown in Fig 9. (b) and the average grain size was about 0.21 µm (about 98.8% reduction in grain size relatively to N=0) due to the fragmentation of the elongated grains during ARB processing. Furthermore, the grain size of the AZ31 layer slightly increased after 6 ARB cycles and ranged between 0.5 and 10 µm. It is known that the new fine grains developed during the ARB processing at the original grain boundaries due to dynamic

recrystallization (DRX) as stated by Stráská et al. (Stráská et al., 2015). Guo et al. (Guo et al., 2016) have reported that recrystallized grains can be classified into two different kinds depending on their location. The first kind is that the new grains are located around large grains and develop a necklace microstructure. This kind of microstructure results mainly from a discontinuous dynamic recrystallization (dDRX) mechanism (Sakai et al., 2014). The second type is the refined grains formed inside shear bands which can be categorized as shear band nucleation recrystallization (sbDRX) (Basu and Al-Samman, 2014). Even though the mechanism is complex, it is generally accepted that the grain refinement of Mg alloys during the ARB processing is the result of dynamic recrystallization (Kumar et al., 2020). It can be speculated that in the present study, a probable mechanism of shear band nucleation recrystallization (sbDRX) should operate since some shear bands have been well evidenced in Fig. 2.e while any trace of necklace-type of recrystallized grains was depicted (Fig.9).

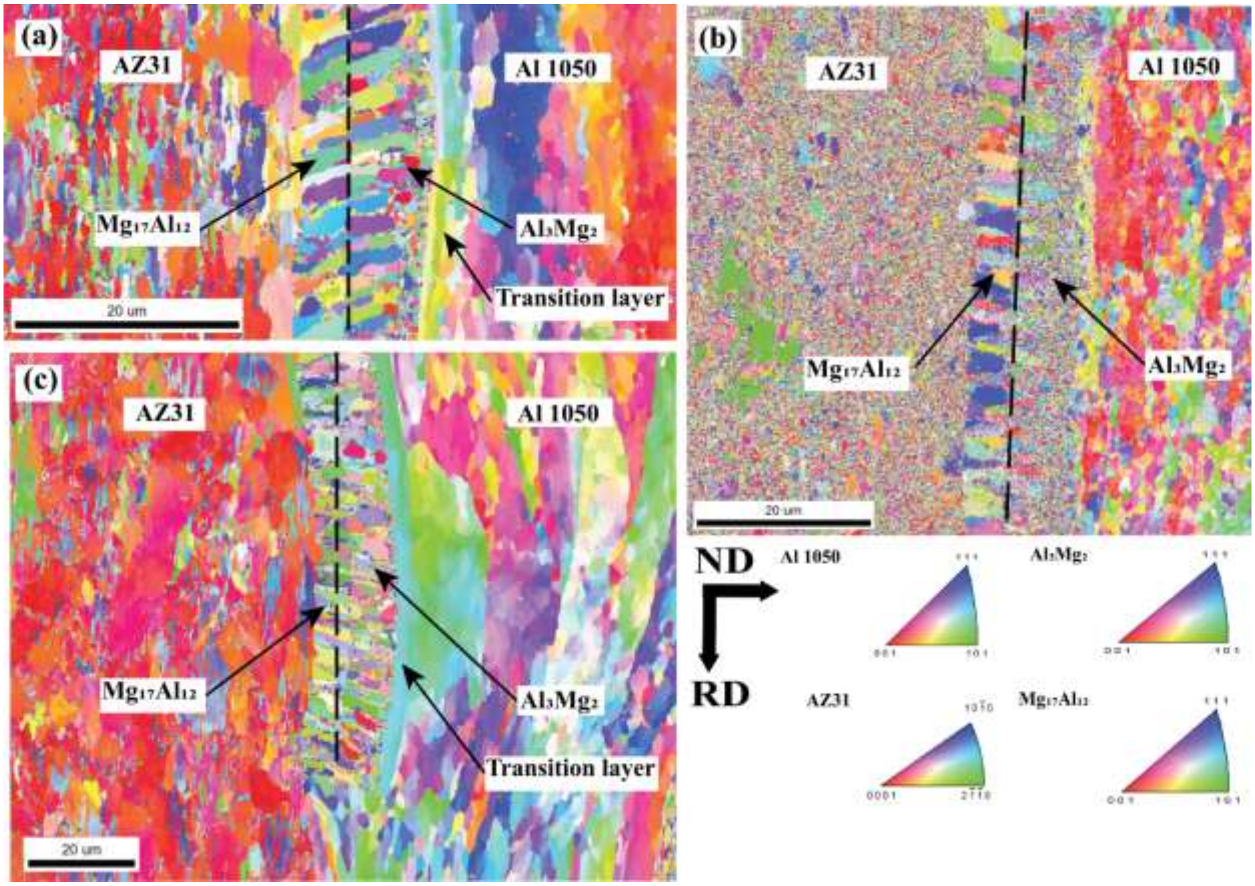

Fig. 9. ND-IPF maps of all phases after a) 2, b) 4, and c) 6 ARB cycles.

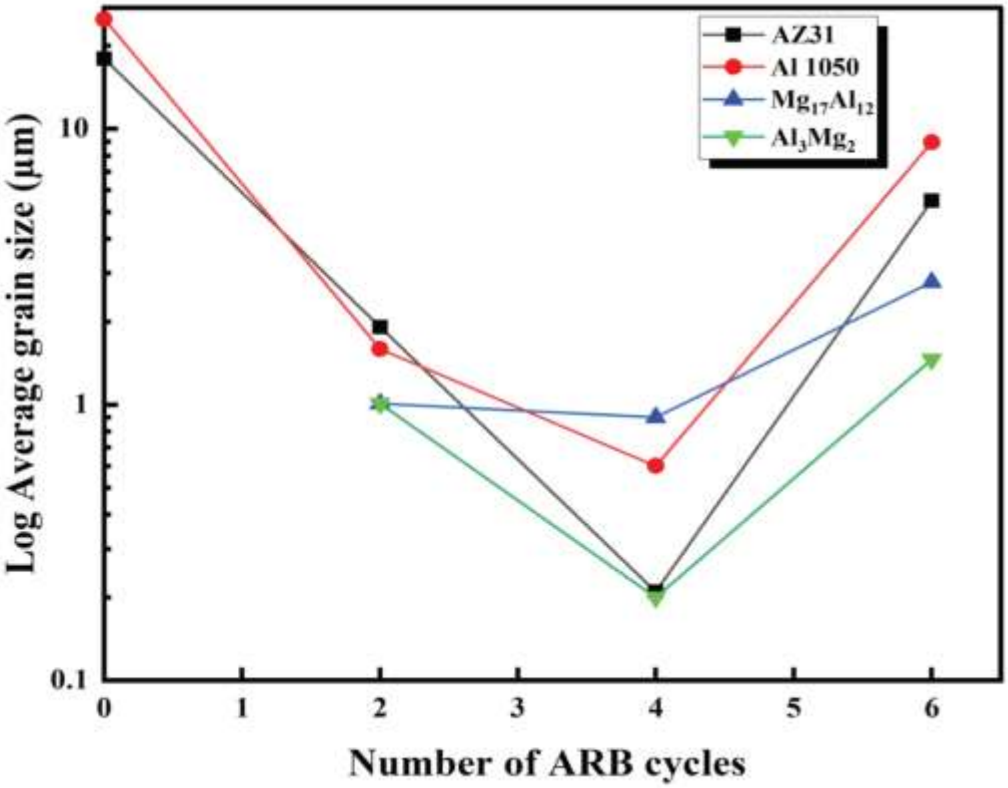

Fig. 10. Average grain size of all phases after different ARB cycles.

When stress levels are high, dynamically recrystallized nuclei develop quickly. During the surface preparation before ARB processing, a certain amount of stress generates due to the wire-brushing. Kumar et al. (Kumar et al., 2020) reported that the dynamic recrystallization during the ARB processing of AZ31 develops more easily at the interface due to the local stress concentration. Indeed, the grain boundaries migrate easily when the processing is undertaken at a high temperature that ensures the cells and subgrains contact and grow.

Concerning the Al 1050 layers at different ARB cycles, the elongated microstructure along the rolling direction is also clearly visible in the IPF maps (Fig. 9). The average grain size reduced to 1.6 and 0.6 μm after 2 and 4 cycles, respectively (Fig.10). However, the average grain size increased to 8.9 μm after 6 cycles which may be caused by the accumulation of large strain within the material and the intermediate annealing during ARB processing which thus promotes the recrystallization and grain growth. The mean grain boundary misorientation angle is 31.6° (the histograms are not shown here) then decreases to reach 13.1° and 12.3° after 4 and 6 ARB cycles, respectively. Simultaneously, the fraction of HAGB increases slowly between one and two ARB cycles from 13 to 15% and then rapidly increases after three cycles to level up after 4 cycles at 23%. However, the high fraction of LAGB within elongated grains after 4 and 6 ARB cycles is normal for any SPD processing which indicates a sub-grains microstructure. It should be noted that the grain refinement process in FCC alloys is not similar to HCP ones. The main mechanism of grain refinement in FCC alloys is characterized by the transformation of LAGBs to HAGBs upon increasing strain (Habila et al., 2019). Nevertheless, grain refinement in FCC materials may be associated with dynamic recrystallization which takes place upon high straining responsible for a drop in LAGB fraction.

The Al_3Mg_2 and $Mg_{17}Al_{12}$ intermetallic compounds which formed after 2 ARB cycles have approximately the same average grain size (1.0 µm) (see Fig. 10). After 4 ARB cycles, the grain refinement of Al_3Mg_2 is more than 4 times higher than $Mg_{17}Al_{12}$. The average grain size of Al_3Mg_2 and $Mg_{17}Al_{12}$ reach 0.2 µm and 0.9 µm, respectively. After 6 cycles of ARB, the average grains size of both Al_3Mg_2 and $Mg_{17}Al_{12}$ increased to 1.5 and 2.8 µm, respectively. However, the Al_3Mg_2 and $Mg_{17}Al_{12}$ IMCs did not exhibit an elongated shape as observed in Al 1050 or AZ31 layers in the rolling directions. Instead, they manifestly present a columnar growth perpendicular to the interface plane. According to Lee et al. (Lee et al., 2012), a columnar growth of the $Mg_{17}Al_{12}$ grains at the interface was mainly induced by the intermediate annealing. Meanwhile, this is a new finding in the Al_3Mg_2 phase since such columnar growth is rarely observed. Lee et al. (Lee et al., 2012) suggested that the columnar growth might be caused by a heat release along the growth direction perpendicular to the interface plane. A similar phenomenon was also observed by Kim et al. (Kim et al., 2015). They reported that the columnar growth could be influenced by the grain size of the substrate alloys. The coarse-grained Mg alloy layer side might promote the coarsening of the $Mg_{17}Al_{12}$ columnar grains. Indeed, Wang et al. (Wang et al., 2020) and Nie et al. (Nie et al., 2019) reported that during annealing, both $Mg_{17}Al_{12}$ and Al_3Mg_2 grains are columnar along the inter-diffusion direction. Wang et al. (Wang et al., 2020) found that the reaction layer contained γ-$Mg_{17}Al_{12}$ layer with columnar grains, and a β-Al_3Mg_2 layer with both rod-like fine-equiaxed grains. The refined Al_3Mg_2 grains near the Al side may be related to the impurities which hindered the growth of the Al_3Mg_2 grains. However, from these previous studies, it is evident that there are several possible grain shapes. The formation mechanism and control methods of grain morphology and size in the reaction layer still need further extensive investigation. Nie et al. (Nie et al., 2019) have investigated the orientation relationship between the IMCs and the matrix using EBSD and TEM. They found that all Al/Al_3Mg_2, Al_3Mg_2/$Mg_{17}Al_{12}$, and $Mg_{17}Al_{12}$/Mg interfaces present a coherent relationship with small misfit degrees ranging from 0.64 to 2.70%. The orientation relationships between them are as follows: $(8\text{-}80)\beta//(141)\gamma$, $(80\text{-}8)\beta//(411)\gamma$, $(01\text{-}\ 1\text{-}1)\mathrm{Mg}//(411)\gamma$ and $(220)\mathrm{Al}//(19, 1, 1)\beta$.

However, in the Al1050/Al_3Mg_2 interfaces, a constitutional transition layer developed. This new layer is seen in Fig 9. (a) and Fig 9. (c) with different colors compared with the Al_3Mg_2 phase layer indicating the supersaturated zone of the Al solid solution which has not yet transformed into an intermetallic compound. The reason behind the development of this transition layer may be referred to as the high nucleation energy of the Al_3Mg_2 phase and may disappear when the intermetallic compound development is significantly enhanced by the governing kinetics (Song et al., 2022; Zhu et al., 2020)**.** Furthermore, Fig. 9(a) shows that the grains of the Al_3Mg_2

IMC are finer than the transitional layer. Contrarily, near the $Mg_{17}Al_{12}$ interface, the Al_3Mg_2 grains can be as coarse as the $Mg_{17}Al_{12}$ ones.

In order to assess the dislocation density of the AZ31, $Mg_{17}Al_{12}$, Al_3Mg_2, and Al1050 layers in the Al1050/AZ31/Al1050 laminated composites upon increasing the ARB cycle number, the KAM method, based on the intergranular misorientations estimation, was used. The KAM value is directly proportional to the dislocation density (Wang et al., 2022). In the present investigation, the KAM maps and the dislocation density measured by the EBSD technique are shown in Fig.11 and Fig12. (a), respectively. After 2 ARB cycles (Fig.12(a)), the dislocation density of the AZ31 layer (1.4×10^{15} m^{-2}) is close to that of Al_3Mg_2 (1.2×10^{15} m^{-2}) and higher compared to those of Al 1050 (9.7×10^{14} m^{-2}) and $Mg_{17}Al_{12}$ (6.2×10^{14} m^{-2}) ones. Basically, the dislocation density after 2 cycles is in the order: $\rho_{AZ31} > \rho_{Al3Mg2} > \rho_{Al\ 1050} > \rho_{Mg17Al12}$. The dislocation density in the zones close to the Al 1050/Al_3Mg_2 interface is higher compared to the dislocation density of Al 1050 or Al_3Mg_2 layers as seen by the stronger green color in the KAM maps (Fig.11 (a)). Therefore, the brittle and hard IMCs layers between dissimilar metal ones are the reason for the significant plastic deformation near the interface. Mo et al. (Mo et al., 2022) reported that the increasing strain gradient led to considerable dislocation pile-up near the interface of the soft 1060Al layer inducing an extra strengthening mechanism due to the tri-metallic Al/Al/Steel composites structure which promoted the improvement of strength and ductility. Subsequently, the dislocation density value of all layers keeps increasing after 4 ARB cycles (Fig.11 (b)) where the presence of red-colored regions increases at this cycle implying an overall increase of the dislocation density. However, a significant gap between the average KAM angle (i.e., dislocation density) of Al_3Mg_2 and AZ31 layers which are 4.1×10^{15} m^{-2} and 2.4×10^{15} m^{-2}, respectively, and a less variation for $Mg_{17}Al_{12}$ and Al 1050 layers which are 1.13×10^{15} m^{-2} and

1.16×10^{15} m^{-2}, respectively, can be noticed. The change in the dislocation density values indicates that more deformation occurs in all layers and now the new hierarchy is $\rho_{Al3Mg2} > \rho_{AZ31} > \rho_{Al\ 1050} \sim \rho_{Mg17Al12}$. Furthermore, the color distribution is non-uniform which reflects that the dislocations are heterogeneously distributed across the microstructure of the Al 1050/AZ31/Al 1050 laminated composite. Evidently, the majority of dislocations were distributed inside the deformed grains and around the substructure after 4 ARB cycles. In the following processing, this high dislocation density will become the starting point of recrystallization. Interestingly, the dislocation density of all layers decreased after 6 ARB cycles. This result indicates that the dislocations generated during the ARB processing are partially annihilated by the DRX mechanism. The most significant dislocation density value is observed at the Al_3Mg_2 and the AZ31 layer after all ARB cycles. Furthermore, most of the dislocations are accumulated near the grain boundaries. Similar results were reported by Zhu et al. (Zhu et al., 2018) for polycrystalline nickel deformed by compression, and Zhi et al. (Zhi et al., 2020) for Fe–22Mn-0.6C TWIP steel deformed by uniaxial tension. Actually, during the ARB processing, the strain rates and the temperature have a significant impact on the activation of the slip systems and the dislocation density variation.

It is worth noting that the present dislocation densities are somewhat higher than those reported in Mg-Er alloys after hot extrusion and annealing. Zhang et al. (Zhang et al., 2023b) stated that the GNDs density of the annealed Mg-Er alloys gradually increased with the increase of strain. Meanwhile the rise of GNDs density is due to intragranular dislocation slip, they believed that slip is a dominant deformation mechanism. The reason of the dislocation density difference is very plausibly due to the alloy processing. Indeed, in the present work, the laminated composites were fabricated by ARB which is a severe plastic deformation while in (Zhang et al., 2023b), the processing is considered as conventional and hence may result in weaker straining. Minor Er and appropriate fine grains would significantly reduce the $CRSS_{non\text{-}basal}/CRSS_{basal}$ ratio, thus contributing to the activation of considerable non-basal dislocations (Zhang et al., 2023b).

Moreover, the dislocation density of the Al_3Mg_2 layer is higher compared to that of the $Mg_{17}Al_{12}$ layer after all ARB cycles. However, when the dislocations are accumulated during severe plastic deformation to a certain level, DRX grains nucleation is promoted with continued deformation and the dislocations will be annihilated by the generated fine DRXed grains. The dislocations develop as a consequence of non-uniform strain at the crystal scale, accommodated by some dislocations during severe plastic deformation and the dislocation density decreases by reducing the degree of lattice curvature (Lee and Jeong, 2023). Usually, a large number of slip bands must be generated when a macro strain needs to be accommodated. As a consequence, the crystallographic orientations of the grains are generally rotated to some extent in order to facilitate slip activation and coordinate the overall deformation (Li et al., 2022). The existence of dislocations near the laminated composite interfaces as well as the grains can be explained by the fact that the profuse grain boundaries as well as solute atoms and precipitates hinder the movement of dislocations, and different crystal orientations also affect the distribution of the dislocation density (Mo et al., 2022). The heterogeneity in the microstructures, texture, and mechanical properties of layers makes them mechanically incompatible during severe plastic deformation, and consequently, produces a significant strain incompatibility at the interfaces during the ARB processing (Mo et al., 2022).

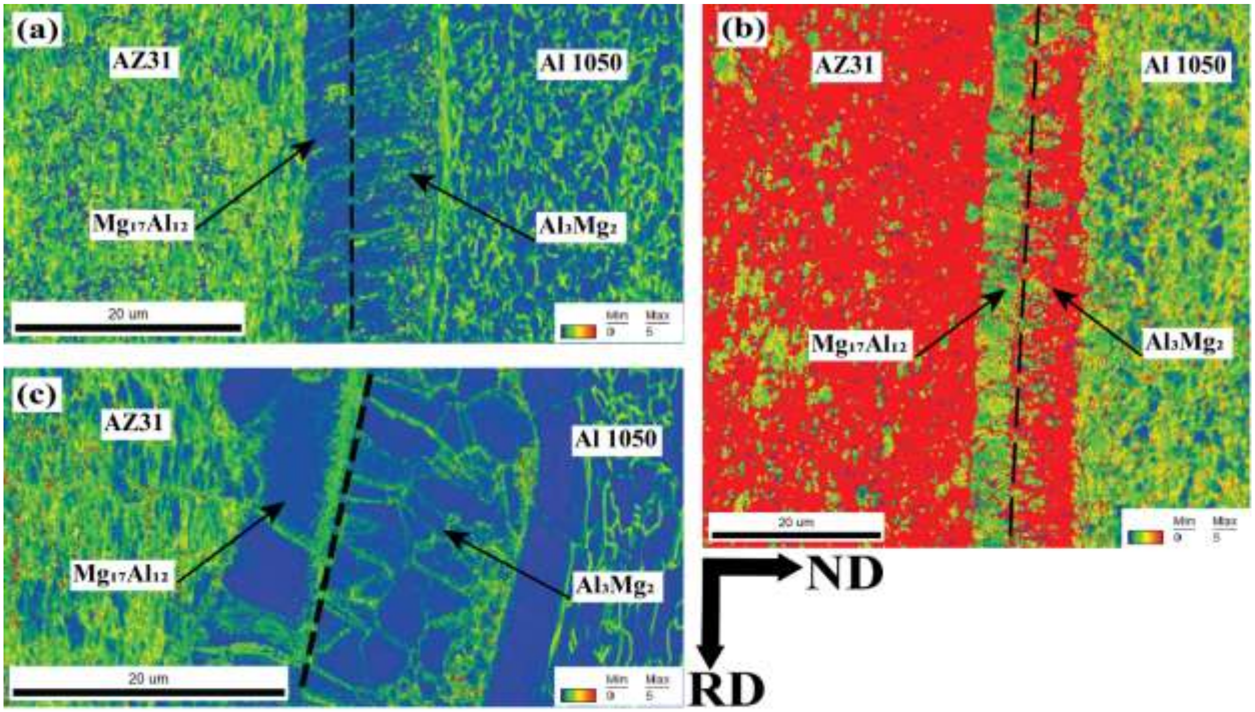

Fig.11. KAM maps of the Al 1050/AZ31/Al 1050 laminated composite after a) 2 cycles, b) 4 cycles, and c) 6 ARB cycles.

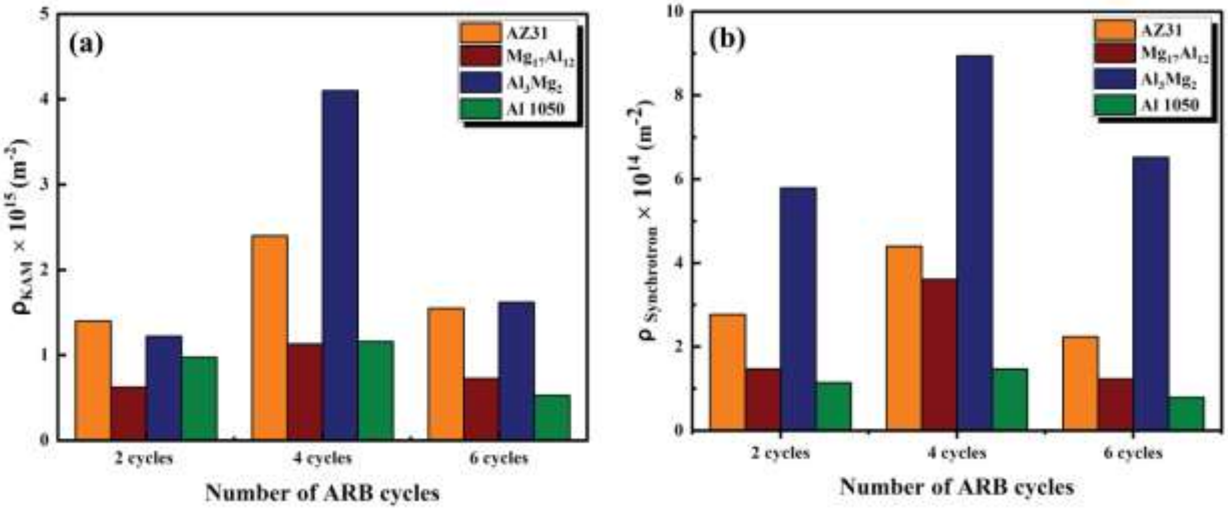

Fig.12. Dislocation density of Al 1050/AZ31/Al 1050 laminated composite after different ARB cycles, a) estimated by EBSD and b) by SXRD.

3.2.Synchrotron X-ray Diffraction (SXRD)

Fig. 13**.** presents a part of diffractograms obtained by SXRD for the Al 1050/AZ31/Al 1050 hybrid composite after N = 2, 4, and 6 ARB cycles. Radiation at 18 keV and the use of a sophisticated and powerful CirPAD detector allowed the collection of the diffracted beam with intensities up to 10^6 cp. /s as well as to reveal characteristics peaks of the intermetallics which are evidently distinct from the background and impossible to resolve using conventional XRD facilities. The part of the diffractograms shows profuse peaks associated with Mg, Al, $Mg_{17}Al_{12}$, and Al_3Mg_2 as well as many other peaks very plausibly ascribed to different complex phases that are present in the AZ31 and Al1050 alloys such as stable Al_3Fe and metastable $Al_xFe_ySi_z$ (Song et al., 2021). These latter were not considered in the present study. The SXRD results confirm the presence of $Mg_{17}Al_{12}$ and Al_3Mg_2 IMCs that formed after N=2 ARB cycles as above shown in Fig. 4. Fig. 12(b) shows the dislocation density measured by SXRD using the Scherrer-Wilson method described in the Experimental Techniques section. The estimated dislocation density of all phases exhibits a similar evolution with those estimated by EBSD (Fig. 12(a)) and consists of almost an increase between N=2 and N=4 followed by a net decrease after N=6. The hierarchy $\rho_{AZ31} > \rho_{Al3Mg2} > \rho_{Al\ 1050} > \rho_{Mg17Al12}$ here is also respected. The dislocation density estimated by using EBSD is slightly higher than those estimated by SXRD. The difference in estimated dislocation density for SXRD and EBSD could be explained by the fact that some dislocations might not be in diffraction conditions. Similar overall trends of the dislocation density of Cu–0.3Cr–0.5Zr subjected to ECAP processing using TEM, EBSD, and X-ray diffraction were reported by Zhilyaev et al. (Zhilyaev et al., 2016). Moreover, Muñoz et al. (Muñoz et al., 2019) stated that many published data show differences in dislocation density values of metals and alloys processed by similar SPD techniques. However, the dislocation density of ARMCO iron processed by ECAP up to a maximum

equivalent strain of sixteen ECAP passes following route Bc determined from EBSD and X-Ray Diffraction Line Profile Analysis, also showed good evolution with present results. The dislocation density of the Al1050 layer accumulated less dislocation upon straining.

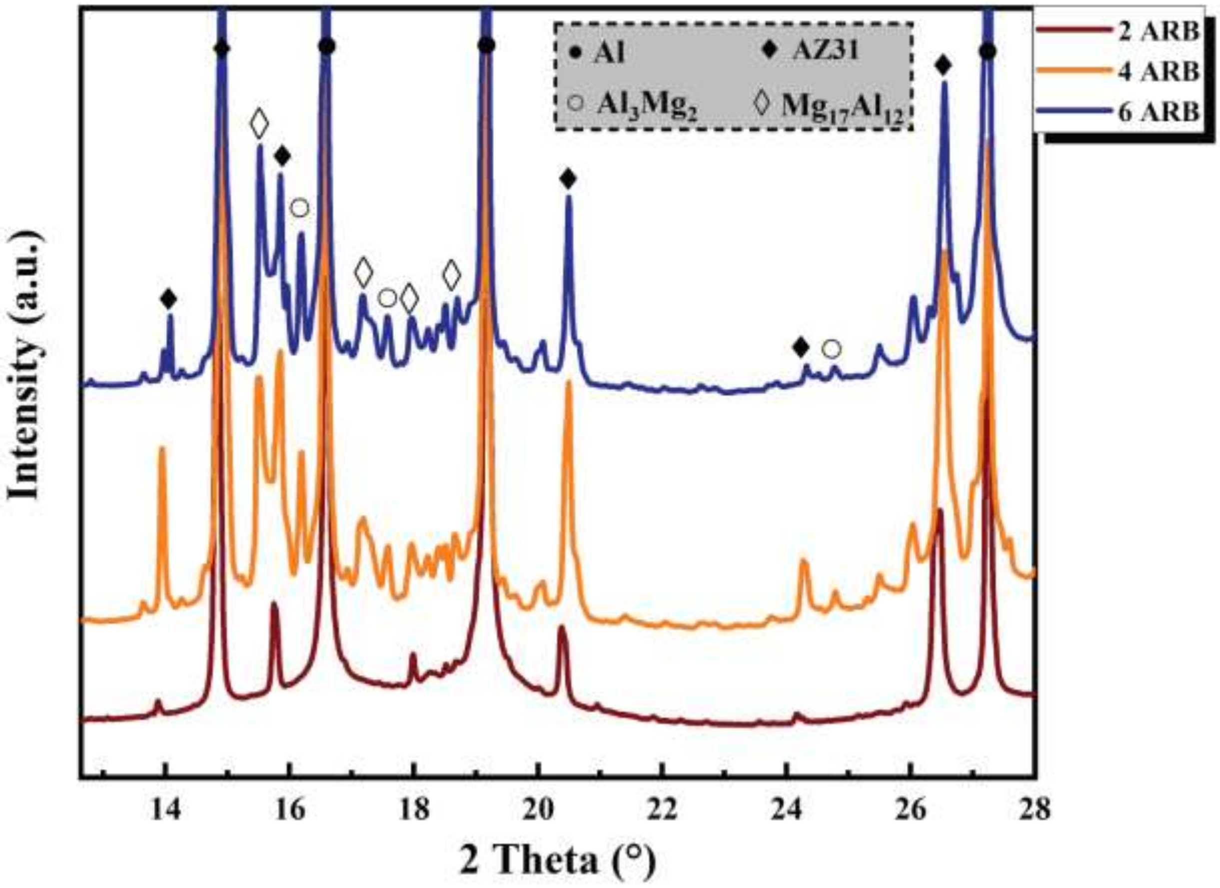

Fig. 13: Part of diffractograms obtained by SXRD for the Al1050/AZ31/Al150 hybrid composite after N=2-6 ARB cycles.

3.3.Texture evolution analysis

Fig. 14 shows the pole figure of the AZ31 layer after different ARB cycles. In hexagonal systems, the orientation of the basal plane with respect to loading is very important to check whether basal slip is geometrically favorable. Hence often, (0002) pole figure is used to describe the texture. Sometimes, (10-10) and (11-20) pole figures are also used to account for any concealed features due to 6-fold symmetry (Hirsch and Al-Samman, 2013; Wang and Huang, 2003). A close inspection of the (10-10) and (11-20) poles figures in the present study did not reveal any additional orientations than those described by the (0002) one. The non-deformed AZ31 alloy texture was of a basal type with basal poles slightly tilting away from the normal direction (ND) towards the transversal direction (TD) with an intensity of 7.4 mrd (not shown here) (Habila et al., 2019). The texture evolution during 2 ARB cycles is illustrated in Fig 14. (a). The (0002) pole figure of the AZ31 layers after 2 cycles exhibits a typical rolling texture of HCP materials with the basal pole tilting slightly away from the normal direction towards the rolling direction and the pole density increased up to 18.9 mrd. This tilt towards the RD direction is proof of the activation of the pyramidal or prismatic glides in HCP systems (Habila et al., 2019). However, basal slip is the main deformation mechanism, and large strain can be accommodated by the material. The rate of recrystallization increases with increasing strain, therefore, helping the basal slip activity. Jeong et al. (Jeong and Ha, 2007) have analyzed the perfect basal texture during the hot rolling of AZ31 alloy and Roostaei et al. (Roostaei et al., 2011) have demonstrated an increase of the basal texture intensity during the annealing of the AZ31 specimen at 350°C. Hence, these studies demonstrated that temperature plays a major impact on the texture evolution of AZ31 alloy during ARB processing. Therefore, in this work, the dynamic recrystallization-assisted deformation could be the main reason for the increase in basal texture intensity in the AZ31 layer after 2 ARB cycles. However, a new texture component ((11-20) < 0001 >) appeared beside the basal texture with increasing ARB cycles as shown in Fig 14. (b) after N=4 ARB cycles. Increasing ARB cycles to N=4 results also a weakening of the texture. The texture weakening could be inferred to dynamic recrystallization where the recrystallized grains may have more favorable orientations for basal slip and consequently will result in texture randomization. Indeed, this decrease in intensity could be also ascribed to shear band formation (Kumar et al., 2020). This indicates that regardless of the initial texture, the texture evolution is largely controlled by the operating deformation mechanism. Kumar et al. (Kumar et al., 2020) have studied the texture evolution of AZ31 alloy in AZ31/AZ31 multilayer and AA5086/AZ31 laminated composite elaborated via ARB processing. The results of this comparative study showed that texture development is strongly affected by the interface in the AZ31/AZ31 multilayer system. They found that the texture intensity of the typical basal texture increased with the rolling reduction. Meanwhile, during the presence of AA5086/AZ31 interfaces, the texture intensity of AZ31 increased initially with rolling reduction and weakened at the higher rolling strain. Based on this study, they concluded that the weakening of texture in AZ31 during the processing at higher strain has been attributed to the development of significant wavy interfaces in AA5086/AZ31 laminated composite. However, the texture evolution after 6 ARB cycles (Fig 14. (c)) is similar to what has already been observed after 2 cycles with higher intensity. Furthermore, the inclination of the basal pole may be related to the activation of pyramidal ⟨c+a⟩ slip and double twins (Huang et al., 2012).

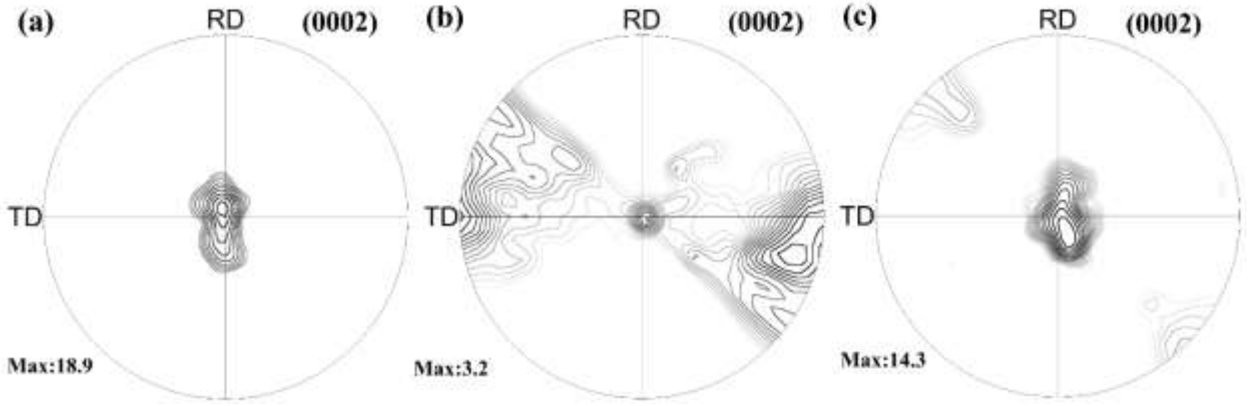

Fig .14. (0002) pole figures of AZ31 layer, a) after 2, b) 4, and c) 6 ARB cycles.

Fig. 15 shows the ODF sections at φ_2 =0, 45, and 65° of the Al 1050 layer after a) 2, b) 4, and c) 6 ARB cycles processing of Al 1050 /AZ31/Al 1050 laminated composite. The principal ideal texture orientations of FCC alloys are also presented. Before ARB processing, the texture of as-received Al 1050 is characterized by a Cube (001) <100> component with an intensity of about 12 multiple random distributions (mrd) (Habila et al., 2019). After 2 ARB cycles (Fig.15 (a)), the Rotated Cube (001) <110> components that is a typical shear texture component was observed with an intensity of 6.9 mrd together with a near S (231) <346> orientation (7.2 mrd). After 4 ARB cycles processing (Fig.15 (b)), the intensity of the Rotated Cube (001) <110> component decreased to 4.9 mrd. After 6 ARB cycles (Fig.15(c)), the Rotated Cube (001) <110> components completely disappeared. Besides, the Cube component and a near Goss component were observed with a weak intensity of about 2.5 mrd and 2.0 mrd, respectively (Fig.16). The Cube orientations are a characteristic component of the recrystallization texture of FCC material sheets (Pirgazi and Akbarzadeh, 2009). The texture change should also be related to the different slip systems that could have been activated during the strain path. Moreover, the shear strain that was mainly introduced by the friction of the rolls and specimen surface may have been responsible for the change in slip pattern too. However, Pirgazi and Akbarzadeh (Pirgazi and Akbarzadeh, 2009) have investigated the texture evolution of AA1100 alloy elaborated by ARB for up to 8 cycles. The results showed that the Rotated Cube component is one of the major components at all cycles while in the current study, the Rotated Cube appeared after 2 cycles and disappeared after 6 cycles. One of the differences between this study and (Pirgazi and Akbarzadeh, 2009) is the temperature which can affect the deformation texture. In this study, the ARB processing was performed at 400°C while it was at 200°C in (Pirgazi and Akbarzadeh, 2009). The second difference is the texture intensity, which decreased after 4 cycles while remaining constant in all cycles in(Pirgazi and Akbarzadeh, 2009). In contrast, Raei et al. (Raei et al., 2010) reported for AA1100 alloy elaborated via ARB up to 6 cycles that all samples show strong β-fiber textures with a sharp Copper orientation. Upon increasing the ARB cycle number, the intensity of the Goss component decreases. In general, it can be concluded that the main factors that highlight the difference between this study and earlier works (Heason and Prangnell, 2002; Pirgazi and Akbarzadeh, 2009; Raei et al., 2010) are: a) deformation temperature, b) annealing conditions, c) rolling parameters (roll diameter, rolling speed, etc.), d) presence of second phase particles and e) position of the texture measurements (near the top surface, mid thickness, and quarter thickness).

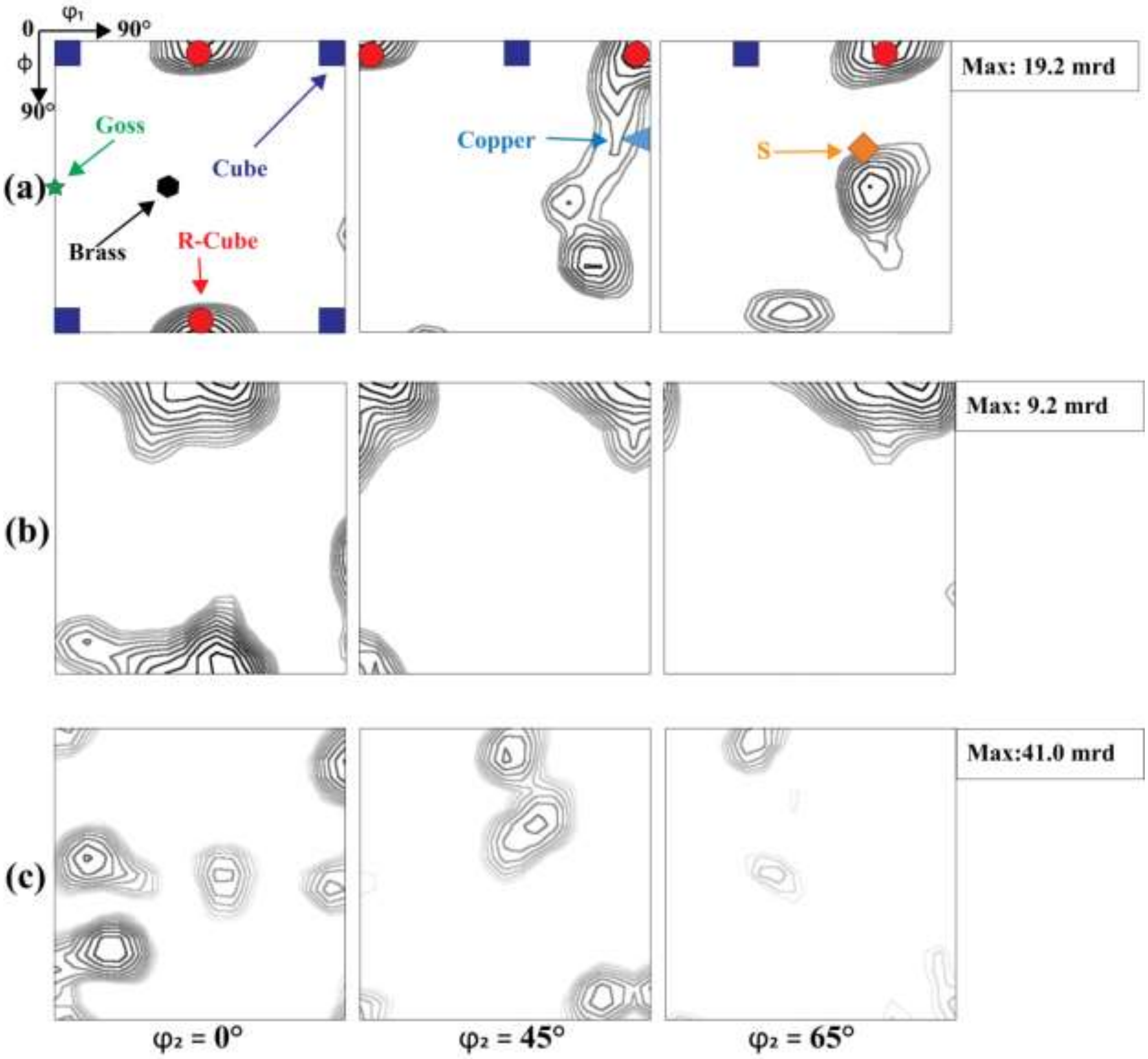

Fig. 15. ODF sections at φ_2 =0, 45 and 65° of the Al 1050 layer after a) 2, b) 4 and c) 6 ARB cycles processing of Al 1050 /AZ31/Al 1050 laminated composite.

In order to interpret the texture evolution of the Al layer in detail, the strength variation of the main texture components is summarized in Fig.17 which reveals the intensity distribution along the α, β- and τ fibers of the Al 1050 layer after different ARB cycles. The major texture components in the deformation of FCC metals and alloys are the α-fiber Goss (110) <001> to rotated Goss (110) <110> (appears in the φ_1 = 0° and 90° sections of the ODF), β-fiber Copper (112) <111> to

Brass (110) <112> (visible in φ_2 = 45° and 90° sections of the ODF) and τ-fiber Rotated Cube (001) <110> to Goss (110) <001> (visible in ϕ= 0° and 90° sections of the ODF). As mentioned above, intensities of the Rotated-Cube intensity dropped (τ-fiber) from N=2 up to N=6 while contrarily, both Cube (θ-fiber, not shown here) and Goss (α-fiber) components got increasing with increasing of the ARB cycles.

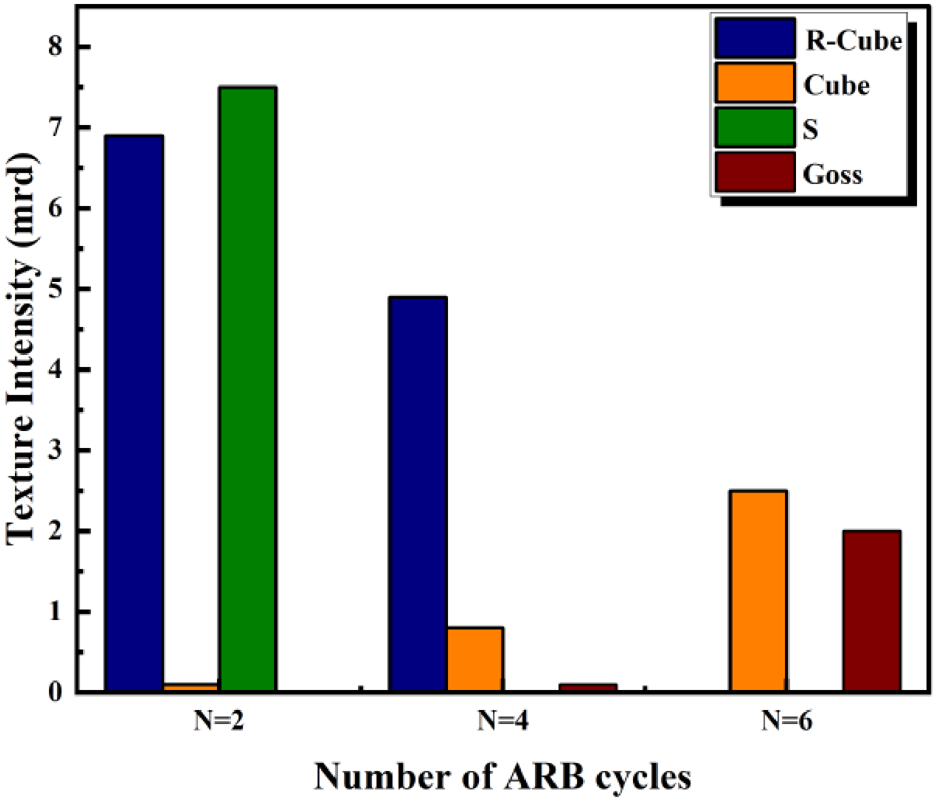

Fig.16. Maximum intensity of the major texture components versus the number of the ARB cycles for the Al 1050 layer.

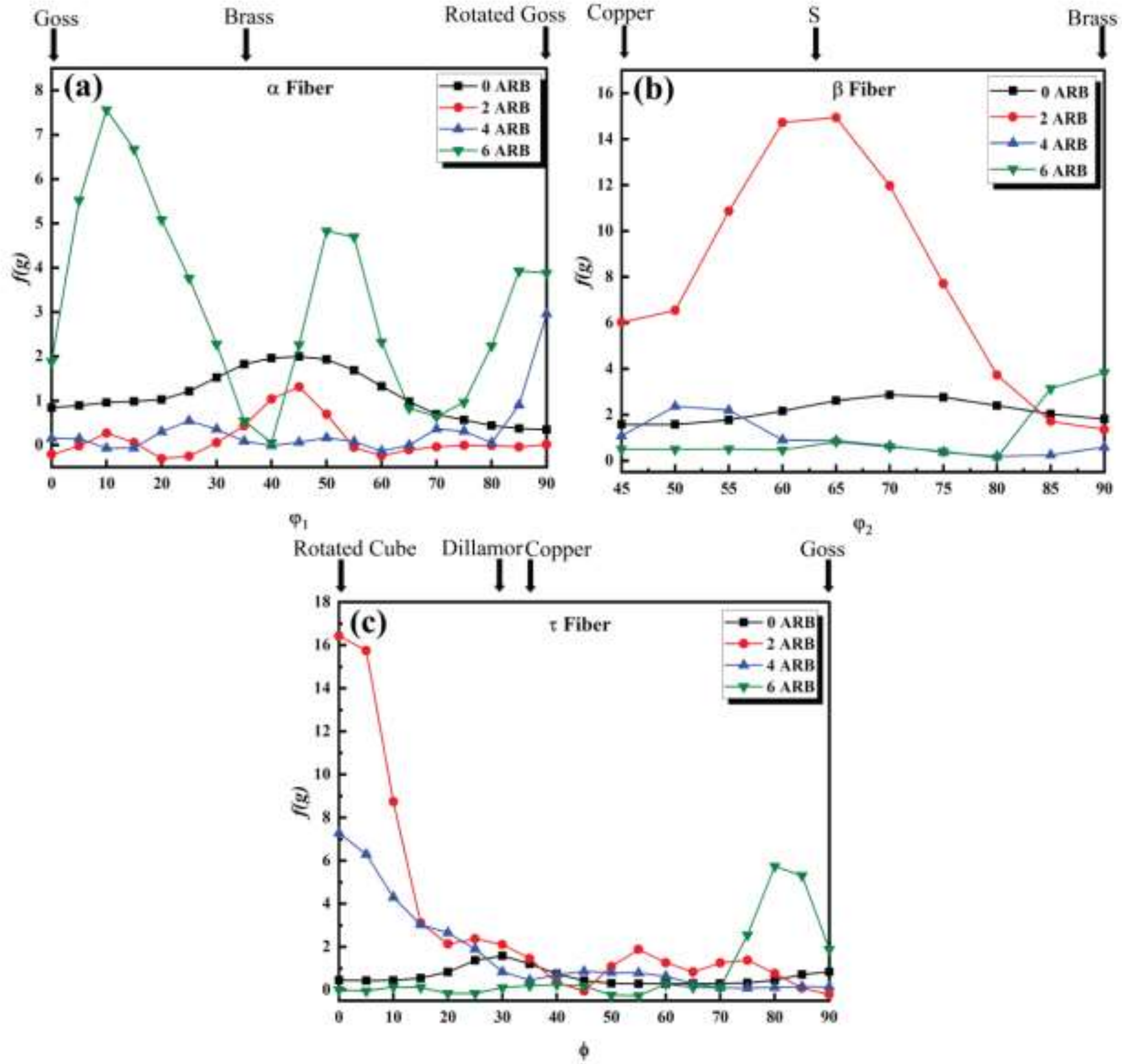

Fig.17. Variation of intensity in the main α-, β- and τ fibers of the Al 1050 layer after different ARB cycles.

Fig.18 illustrates the texture evolution of the Al_3Mg_2 and $Mg_{17}Al_{12}$ intermetallic phases after different ARB cycles in terms of (111) recalculated pole figures obtained from EBSD measurements. Due to the small numbers of grains, a manifest random texture is depicted for all cycles, indicating that the intermetallic phases failed to develop preferred crystallographic orientations. This has been already assumed by Wang et al.(Wang and Prangnell, 2017). However, because of the poor statistics (very faint number of analyzed grains), it is difficult to conclude about the existence of Copper, Brass, S, or any other type orientations. Lychagina et al. (Lychagina and Nikolayev, 2003) have investigated the minimum suitability of grains for quantitative texture analysis. In this work (Lychagina and Nikolayev, 2003), the authors reported that the minimum number of grains for conventional averaging is about 8 000 for cubic symmetry and about 10 000 for hexagonal symmetry. The present study concerns intermetallics with microstructures far from these grain numbers.

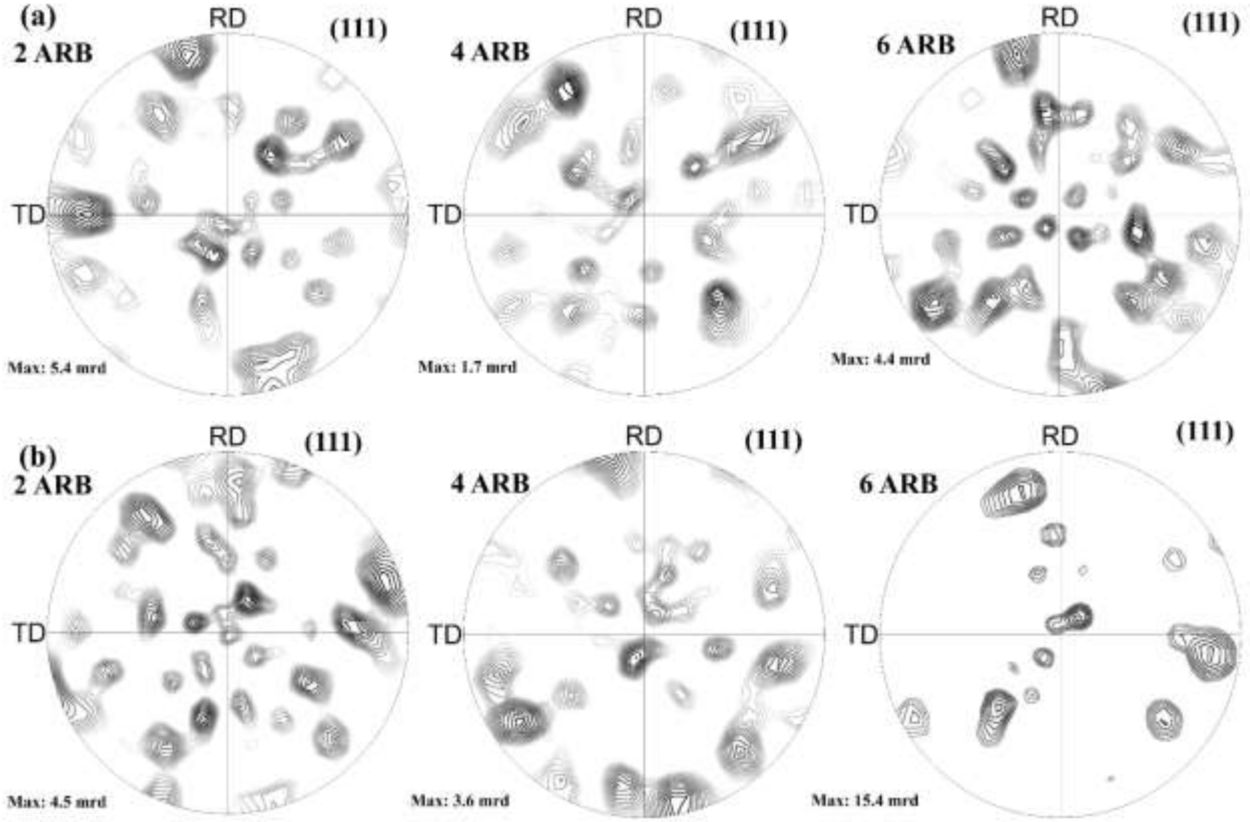

Fig. 18. (111) pole figures representing data coming from the IPF EBSD maps for the intermetallic compounds after different ARB cycles (a) Al_3Mg_2, (b) $Mg_{17}Al_{12}$

4. Conclusion

The Al 1050/AZ31/Al 1050 multilayered composite elaborated via the ARB processing at 400 °C, up to 6 cycles led to the formation of Al_3Mg_2 and $Mg_{17}Al_{12}$ intermetallic compounds. The evolution of microstructure and texture derived from EBSD and SXRD investigations suggest the following conclusions :

- EBSD and SXRD analyses confirmed the formation of $Mg_{17}Al_{12}$ and Al_3Mg_2 phases near the interface bonding soon after N=2 cycles.
- The polycrystalline intermetallic plates' growth was columnar and normal to the bonding interface.
- The Al_3Mg_2 and $Mg_{17}Al_{12}$ intermetallic compounds have the same average grain size (1.0 µm) after 2 ARB cycles. After 4 ARB cycles, the grain refinement of Al_3Mg_2 is more than 4 times higher than in $Mg_{17}Al_{12}$. The average grain size of Al_3Mg_2 and $Mg_{17}Al_{12}$ reach 0.2 and 0.9 µm, respectively.
- The dislocation density obeyed this hierarchy after N=4 and 6 ARB cycles $\rho_{Al3Mg2} > \rho_{AZ31} > \rho_{Al\ 1050} \sim \rho_{Mg17Al12}$ and the Al_3Mg_2 IMCs were shown to store more dislocations.
- A typical strong basal (0002) texture has been observed in the AZ31 layer and a weak rolling texture showed in Al 1050 layer with the domination of the Rotated Cube (001) <110> component.
- The $Mg_{17}Al_{12}$ and Al_3Mg_2 intermetallics plates did not exhibit any preferential orientations.

Acknowledgments

The authors are warmly thanking Dr-Ing. Norbert Hort and Dr. Dietmar Letzig from MagIC - Magnesium Innovations Center, Germany, for kindly providing the AZ31 alloy. The authors would also like to thank Dr. M.A. Benhmeida from the Faculty of Foreign Languages, University of Mostaganem, Algeria, for English improvement.

Declaration of Competing Interest:

The authors declare that they have no known competing financial interests or personal relationships that could have appeared to influence the work reported in this paper.

Data availability:

The raw/processing data required to reproduce these findings cannot be shared at this time, as the data also forms part of an ongoing study.

References

Acarer, M., Demir, B., Dikici, B., Salur, E., 2022. Microstructure, mechanical properties, and corrosion resistance of an explosively welded Mg–Al composite. J. Magnes. Alloy. 10, 1086–1095. https://doi.org/10.1016/j.jma.2021.08.009

Azzeddine, H., Bourezg, Y.I., Khereddine, A.Y., Baudin, T., Helbert, A.L., Brisset, F., Kawasaki, M., Bradai, D., Langdon, T.G., 2020. An investigation of the stored energy and thermal stability in a Cu–Ni–Si alloy processed by high-pressure torsion. Philos. Mag. 100, 688–712. https://doi.org/10.1080/14786435.2019.1703055

Basak, M., Rahman, L., Ahmed, F., Biswas, B., Sharmin, N., 2022. The use of X-ray diffraction peak profile analysis to determine the structural parameters of cobalt ferrite nanoparticles using DebyeScherrer, Williamson-Hall, Halder-Wagner and Size-strain plot: Different precipitating agent approach. J. Alloys Compd. 895, 162694.

Basu, I., Al-Samman, T., 2014. Triggering rare earth texture modification in magnesium alloys by addition of zinc and zirconium. Acta Mater. 67, 116–133. https://doi.org/10.1016/j.actamat.2013.12.015

Bay, B., Hansen, N., Hughes, D.A., Kuhlmann-Wilsdorf, D., 1992. Overview no. 96 evolution of f.c.c. deformation structures in polyslip 40, 205–219. https://doi.org/https://doi-org.sndl1.arn.dz/10.1016/0956-7151(92)90296-Q

Beygi, R., Pouraliakbar, H., Torabi, K., B, G.E., Fallah, V., Kim, S.K., Shi, R., Silva, L.F.M. da, 2021. The inhibitory effect of stir zone liquefaction and eutectic-phase formation on the growth of γ_β intermetallics during dissimilar FSW of Al_Mg alloys.pdf. J. Manuf. Process. 70, 152–162. https://doi.org/10.1016/j.jmapro.2021.08.049

Boon, Y. Di, Joshi, S.C., 2020. A review of methods for improving interlaminar interfaces and fracture toughness of laminated composites. Mater. Today Commun. 22. https://doi.org/10.1016/j.mtcomm.2019.100830

Chen, B., Wang, Y., Xiao, C., Zhang, M., Ni, G., Li, D., 2018. The formation mechanism of intermetallic compounds in Al/Mg friction-stir weld joint. Mater. Sci. Technol. (United Kingdom) 34, 703–711. https://doi.org/10.1080/02670836.2017.1410926

Chen, M., Hsieh, C., Wu, W., 2007. Metals and Materials International Volume 13 issue 3 2007 [doi 10.1007_bf03027805] Ming-Che Chen; Chih-Chun Hsieh; Weite Wu -- Microstructural characterization of AlMg allo.pdf 13, 201–205.

Desjardins, K., Mocuta, C., Dawiec, A., Réguer, S., Joly, P., Dubuisson, J.M., Alves, F., Noureddine, A., Bompard, F., Thiaudière, D., 2022. The CirPAD, a circular 1.4 M hybrid pixel detector dedicated to X-ray diffraction measurements at Synchrotron SOLEIL. J. Synchrotron Radiat. 29, 180–193. https://doi.org/10.1107/S1600577521012492

E, B., B, A., A, A., 2016. Chapter 9 Nano structures by severe plastic deformation (SPD) processes. In: Applied mathematical models experimental approaches chemical science. Apple Academic Press. https://doi.org/https:// doi.org/10.1201/9781315366203

Gerlich, A., Su, P., North, T.H., 2005. Peak temperatures and microstructures in aluminium and magnesium alloy friction stir spot welds. Sci. Technol. Weld. Join. 10, 647–652. https://doi.org/10.1179/174329305X48383

Guan, F., Jiang, W., Li, G., Zhu, J., Wang, J., Jie, G., Fan, Z., 2022. Effect of vibration on interfacial microstructure and mechanical properties of Mg/Al bimetal prepared by a novel compound casting. J. Magnes. Alloy. 10, 2296–2309. https://doi.org/10.1016/j.jma.2021.11.023

Guo, F., Zhang, D., Fan, X., Jiang, L., Yu, D., Pan, F., 2016. Deformation behavior of AZ31 Mg alloys sheet during large strain hot rolling process: A study on microstructure and texture evolutions of an intermediate-rolled sheet. J. Alloys Compd. 663, 140–147. https://doi.org/10.1016/j.jallcom.2015.12.063

Guo, Y., Quan, G., Ren, L., Liu, B., Al-Ezzi, S., Pan, H., 2019. Effect of Zn interlayer thickness on the microstructure and mechanical properties of two-step diffusion bonded joint of ZK60Mg and 5083Al. Vacuum 161, 353–360. https://doi.org/10.1016/j.vacuum.2018.12.036

Habila, W., Azzeddine, H., Mehdi, B., Tirsatine, K., Baudin, T., Helbert, A.L., Brisset, F., Gautrot, S., Mathon, M.H., Bradai, D., 2019. Investigation of microstructure and texture evolution of a Mg/Al laminated composite elaborated by accumulative roll bonding. Mater. Charact. 147, 242–252. https://doi.org/10.1016/j.matchar.2018.11.010

Haddadi, F., 2015. Rapid intermetallic growth under high strain rate deformation during high power ultrasonic spot welding of aluminium to steel. Mater. Des. 66, 459–472. https://doi.org/10.1016/j.matdes.2014.07.001

Heason, C.P., Prangnell, P.B., 2002. Grain refinement and texture evolution during the deformation of Al to ultra-high strains by accumulative roll bonding (ARB). Mater. Sci. Forum 396–402, 429–434. https://doi.org/10.4028/www.scientific.net/msf.396-402.429

Hebert, R.J., Perepezko, J.H., 2004. Deformation-induced synthesis and structural transformations of metallic multilayers. Scr. Mater. 50, 807–812. https://doi.org/10.1016/j.scriptamat.2003.11.047

Hirsch, J., Al-Samman, T., 2013. Superior light metals by texture engineering: Optimized aluminum and magnesium alloys for automotive applications. Acta Mater. 61, 818–843. https://doi.org/10.1016/j.actamat.2012.10.044

Huang, X., Suzuki, K., Chino, Y., Mabuchi, M., 2012. Influence of initial texture on rolling and annealing textures of Mg-3Al-1Zn alloy sheets processed by high temperature rolling. J. Alloys Compd. 537, 80–86. https://doi.org/10.1016/j.jallcom.2012.05.002

Jeong, H.T., Ha, T.K., 2007. Texture development in a warm rolled AZ31 magnesium alloy. J. Mater. Process. Technol. 187–188, 559–561. https://doi.org/10.1016/j.jmatprotec.2006.11.084

Jiang, S., Peng, R.L., An, K., Yan, H.L., Zhao, X., Zuo, L., Cui, W.B., Esling, C., Jia, N., 2022. Unraveling dislocation-type evolution dominated strain hardening in laminated Ti/Nb composites. Mater. Sci. Eng. A 851. https://doi.org/10.1016/j.msea.2022.143620

Kapoor, K., Lahiri, D., Batra, I.S., Rao, S.V.R., Sanyal, T., 2005. X-ray diffraction line profile analysis for defect study in Cu-1 wt.% Cr-0.1 wt.% Zr alloy. Mater. Charact. 54, 131–140. https://doi.org/10.1016/j.matchar.2004.09.009

Kim, J.S., Lee, K.S., Kwon, Y.N., Lee, B.J., Chang, Y.W., Lee, S., 2015. Improvement of interfacial bonding strength in roll-bonded Mg/Al clad sheets through annealing and secondary rolling process. Mater. Sci. Eng. A 628, 1–10. https://doi.org/10.1016/j.msea.2015.01.035

Kumar, P., Madhup, A., Kalvala, P.R., Suwas, S., 2020. Texture evaluation in AZ31/AZ31 multilayer and AZ31/AA5068 laminar composite during accumulative roll bonding. Def. Technol. 16, 514–519. https://doi.org/10.1016/j.dt.2019.08.014

Lee, G.M., Lee, J.U., Park, S.H., 2022. Variation in bending deformation behavior and improvement in bendability of extruded pure Mg through Gd addition. Mater. Sci. Eng. A 855. https://doi.org/10.1016/j.msea.2022.143940

Lee, J., Jeong, H., 2023. Effect of the annealing process on the formation and growth of intermetallic compounds at the interface of Cu clad Al wire drawn with high area reduction. Mater. Lett. 331, 133474. https://doi.org/10.1016/j.matlet.2022.133474

Lee, K.S., Yoon, D.H., Kim, H.K., Kwon, Y.N., Lee, Y.S., 2012. Effect of annealing on the interface microstructure and mechanical properties of a STS-Al-Mg 3-ply clad sheet. Mater. Sci. Eng. A 556, 319–330. https://doi.org/10.1016/j.msea.2012.06.094

Li, C., Chi, C., Lin, P., Zhang, H., Liang, W., 2015. Deformation behavior and interface microstructure evolution of Al/Mg/Al multilayer composite sheets during deep drawing. Mater. Des. 77, 15–24. https://doi.org/10.1016/j.matdes.2015.03.034

Li, Z., Lin, Y.C., Zhang, L., Zheng, J., Zhao, J., Wang, R., Jiang, Z., 2022. In-situ investigation on tensile properties of a novel Ti/Al composite sheet. Int. J. Mech. Sci. 231. https://doi.org/10.1016/j.ijmecsci.2022.107592

Lychagina, T.A., Nikolayev, D.I., 2003. Model investigation of the grain number to apply quantitative texture analysis averaging. Phys. Status Solidi Appl. Res. 195, 322–334. https://doi.org/10.1002/pssa.200305925

Malinov, S., Sha, W., Guo, Z., Tang, C.C., Long, A.E., 2002. Synchrotron X-ray diffraction study of the phase transformations in titanium alloys. Mater. Charact. 48 48, 279–295. https://doi.org/https://doi.org/10.1016/S1044-5803(02)00286-3

Mansouri, H., Eghbali, B., Afrand, M., 2019. Producing multi-layer composite of stainless steel/aluminum/copper by accumulative roll bonding (ARB) process. J. Manuf. Process. 46, 298–303. https://doi.org/10.1016/j.jmapro.2019.08.025

Mo, T., Xiao, H., Lin, B., Li, W., Wang, P., Ma, K., 2022. Improvement of mechanical properties of tri-metallic 7075Al/1060Al/304 SS composite via collaborative strengthening behavior. Mater. Sci. Eng. A 857. https://doi.org/10.1016/j.msea.2022.144072

Mokhles, M., Hosseini, M., Danesh-Manesh, H., Zebarjad, S.M., 2020. Structure and mechanical properties of Ni/Ti multilayered composites produced by accumulative roll-bonding process. J. Compos. Mater. 54, 1119–1126. https://doi.org/10.1177/0021998319874391

Muñoz, J.A., Higuera, O.F., Benito, J.A., Bradai, D., Khelfa, T., Bolmaro, R.E., Jorge, A.M., Cabrera, J.M., 2019. Analysis of the micro and substructural evolution during severe plastic deformation of ARMCO iron and consequences in mechanical properties. Mater. Sci. Eng. A 740–741, 108–120. https://doi.org/10.1016/j.msea.2018.10.100

Muránsky, O., Balogh, L., Tran, M., Hamelin, C.J., Park, J.S., Daymond, M.R., 2019. On the measurement of dislocations and dislocation substructures using EBSD and HRSD techniques. Acta Mater. 175, 297–313. https://doi.org/10.1016/j.actamat.2019.05.036

Nie, H., Liang, W., Chen, H., Wang, F., Li, T., Chi, C., Li, X. rong, 2019. A coupled EBSD/TEM study on the interfacial structure of Al/Mg/Al laminates. J. Alloys Compd. 781, 696–701. https://doi.org/10.1016/j.jallcom.2018.11.366

Nie, H., Liang, W., Chen, H., Zheng, L., Chi, C., Li, X., 2018. Effect of annealing on the microstructures and mechanical properties of Al/Mg/Al laminates. Mater. Sci. Eng. A 732, 6–13. https://doi.org/10.1016/j.msea.2018.06.065

Ohsaki, S., Kato, S., Tsuji, N., Ohkubo, T., Hono, K., 2007. Bulk mechanical alloying of Cu-Ag and Cu/Zr two-phase microstructures by accumulative roll-bonding process. Acta Mater. 55, 2885–2895. https://doi.org/10.1016/j.actamat.2006.12.027

Panteli, A., Robson, J.D., Brough, I., Prangnell, P.B., 2012. The effect of high strain rate deformation on intermetallic reaction during ultrasonic welding aluminium to magnesium. Mater. Sci. Eng. A 556, 31–42. https://doi.org/10.1016/j.msea.2012.06.055

Pirgazi, H., Akbarzadeh, A., 2009. Role of second phase particles on microstructure and texture evolution of ARB processed aluminium sheets. Mater. Sci. Technol. 25, 625–631. https://doi.org/10.1179/174328408X332771

Raei, M., Toroghinejad, M.R., Jamaati, R., Szpunar, J.A., 2010. Effect of ARB process on textural evolution of AA1100 aluminum alloy. Mater. Sci. Eng. A 527, 7068–7073. https://doi.org/10.1016/j.msea.2010.07.089

Rahmatabadi, D., Tayyebi, M., Hashemi, R., Faraji, G., 2018. Microstructure and mechanical properties of Al/Cu/Mg laminated composite sheets produced by the ARB proces. Int. J. Miner. Metall. Mater. 25, 564–572. https://doi.org/10.1007/s12613-018-1603-x

Ren, R., Fan, J., Wang, B., Zhang, Q., Li, W., Dong, H., 2022. Hall-Petch relationship and deformation mechanism of pure Mg at room temperature. J. Alloys Compd. 920, 1–11. https://doi.org/https://doi.org/10.1016/j.jallcom.2022.165924

Roostaei, A.A., Zarei-Hanzaki, A., Abedi, H.R., Rokni, M.R., 2011. An investigation into the mechanical behavior and microstructural evolution of the accumulative roll bonded AZ31 Mg alloy upon annealing. Mater. Des. 32, 2963–2968. https://doi.org/10.1016/j.matdes.2011.01.038

Sakai, T., Belyakov, A., Kaibyshev, R., Miura, H., Jonas, J.J., 2014. Dynamic and post-dynamic recrystallization under hot, cold and severe plastic deformation conditions. Prog. Mater. Sci. 60, 130–207. https://doi.org/10.1016/j.pmatsci.2013.09.002

Sato, Y.S., Park, S.H.C., Michiuchi, M., Kokawa, H., 2004. Constitutional liquation during dissimilar friction stir welding of Al and Mg alloys. Scr. Mater. 50, 1233–1236.

https://doi.org/10.1016/j.scriptamat.2004.02.002

Song, K., Liu, X., Ji, Y., Wei, Y., Luo, J., Liu, F., Liu, D., Zhong, Z., 2022. Intermetallic Compounds (IMCs) Formation in Al/Mg Dissimilar Alloy Solid State Joining: Experimental Study and Phase Field Modeling. Met. Mater. Int. https://doi.org/10.1007/s12540-022-01292-8

Song, Z., Magdysyukb, O. V., Tanga, L., Sparksa, T., Caia, B., 2021. Growth dynamics of faceted Al13Fe4 intermetallic revealed by high-speed synchrotron X-ray quantification. J. Alloys Compd. 861, 158604. https://doi.org/https://doi.org/10.1016/j.jallcom.2021.158604

Stokes, A.R., Wilson, A.J.C., 1944. The diffraction of x rays by distorted crystal aggregates - I. Proc. Phys. Soc. 56, 174–181. https://doi.org/10.1088/0959-5309/56/3/303

Stráská, J., Janeček, M., Gubicza, J., Krajňák, T., Yoon, E.Y., Kim, H.S., 2015. Evolution of microstructure and hardness in AZ31 alloy processed by high pressure torsion. Mater. Sci. Eng. A 625, 98–106. https://doi.org/10.1016/j.msea.2014.12.005

Straumal, B.B., Kilmametov, A.R., Ivanisenko, Y., Mazilkin, A.A., Kogtenkova, O.A., Kurmanaeva, L., Korneva, A., Zie, P., Baretzky, B., 2015. Phase transitions inducedbysevere plastic deformation: steady-stateand equifinality. Int. J. Mater. Res. 106, 657–664.

Vaid, A., Guénolé, J., Prakash, A., Korte-Kerzel, S., Bitzek, E., 2019. Atomistic simulations of basal dislocations in Mg interacting with Mg17Al12 precipitates. Materialia 7. https://doi.org/10.1016/j.mtla.2019.100355

Verstraete, K., Prévond, L., Helbert, A.L., Baudin, T., 2019. Magnetic Shielding at Low Frequencies: Application for an Aluminum/Steel Composite Elaborated by Accumulative Roll Bonding. Adv. Eng. Mater. 21, 1–8. https://doi.org/10.1002/adem.201800967

Wang, H., Ma, J., Yuan, M., Liang, G., Pei, X., Miao, Y., Li, M., 2022. Microstructure, deformation behaviors and GND density evolution of Ti-Al laminated composites under the incremental compression test. Mater. Today Commun. 33, 1–9. https://doi.org/10.1016/j.mtcomm.2022.104605

Wang, L., Wang, Y., Prangnell, P., Robson, J., 2015. Modeling of Intermetallic Compounds Growth Between Dissimilar Metals. Metall. Mater. Trans. A Phys. Metall. Mater. Sci. 46, 4106–4114. https://doi.org/10.1007/s11661-015-3037-7

Wang, P., Chen, Z., Hu, C., Li, B., Lin, J., Liu, Q., 2020. Effects of annealing on the interfacial structures and mechanical properties of hot roll bonded Al/Mg clad sheets. Mater. Sci. Eng. A 792, 139673. https://doi.org/https://doi.org/10.1016/j.msea.2020.139673

Wang, Y., Prangnell, P.B., 2017. The significance of intermetallic compounds formed during interdiffusion in aluminum and magnesium dissimilar welds. Mater. Charact. 134, 84–95. https://doi.org/10.1016/j.matchar.2017.09.040

Wang, Y.N., Huang, J.C., 2003. Texture analysis in hexagonal materials. Mater. Chem. Phys. 81, 11–26. https://doi.org/10.1016/S0254-0584(03)00168-8

Wen, M., Chen, M., 2014. Comparative study on plastic deformation of nanocrystalline Al and

Ni. Metall. Mater. Trans. A Phys. Metall. Mater. Sci. 45, 1631–1638. https://doi.org/10.1007/s11661-013-2076-1

Xie, J., Wang, L., Zhang, J., Lu, L., Zhang, Z., He, Y., Wu, R., 2023a. Developing new Mg alloy as potential bone repair material via constructing weak anode nano-lamellar structure. J. Magnes. Alloy. 11, 154–175. https://doi.org/10.1016/j.jma.2022.08.011

Xie, J., Zhang, J., Zhang, Z., Yu, Z., Xu, Z., Wang, R., Fang, D., Zhang, Xiaobo, Zhang, Xiaoru, Wu, R., 2023b. Corrosion mechanism of Mg alloys involving elongated long-period stacking ordered phase and intragranular lamellar structure. J. Mater. Sci. Technol. 151, 190–203. https://doi.org/10.1016/j.jmst.2023.01.005

Yang, D., Cizek, P., Hodgson, P., Wen, C., 2010. Ultrafine equiaxed-grain Ti/Al composite produced by accumulative roll bonding. Scr. Mater. 62, 321–324. https://doi.org/10.1016/j.scriptamat.2009.11.036

Yu, J., Zhou, W., Zhao, G., 2021. Influence of strain, temperature, and strain rate on interfacial structure and strength of AZ31BMg/6063Al formed by plastic deformation bonding. J. Manuf. Process. 65, 299–311. https://doi.org/10.1016/j.jmapro.2021.03.026

Zhang, R., Acoff, V.L., 2007. Processing sheet materials by accumulative roll bonding and reaction annealing from Ti/Al/Nb elemental foils. Mater. Sci. Eng. A 463, 67–73. https://doi.org/10.1016/j.msea.2006.06.144

Zhang, Z., Xie, J., Zhang, J., Dong, H., Liu, S., Zhang, X., Wang, J., Wu, R., 2023a. Simultaneously improving mechanical and anti-corrosion properties of extruded Mg-Al dilute alloy via trace Er addition. J. Mater. Sci. Technol. 150, 49–64. https://doi.org/10.1016/j.jmst.2022.12.014

Zhang, Z., Zhang, J., Xie, J., Liu, S., Fu, W., Wu, R., 2023b. Developing a Mg alloy with ultrahigh room temperature ductility via grain boundary segregation and activation of non-basal slips. Int. J. Plast. 162. https://doi.org/10.1016/j.ijplas.2023.103548

Zhao, Y., Luo, Y., Lu, Y., He, Y., Guo, X., Wang, S., Cui, H., Zhang, Y., Wang, Z., 2021. Effect of welding parameters on the microstructures and mechanical properties of double-pass aluminum/magnesium dissimilar metal friction stir lap welding joint. Mater. Today Commun. 26, 102132. https://doi.org/10.1016/j.mtcomm.2021.102132

Zhi, H., Zhang, C., Antonov, S., Yu, H., Guo, T., Su, Y., 2020. Investigations of dislocation-type evolution and strain hardening during mechanical twinning in Fe-22Mn-0.6C twinning-induced plasticity steel. Acta Mater. 195, 371–382. https://doi.org/10.1016/j.actamat.2020.05.062

Zhilyaev, A.P., Shakhova, I., Morozova, A., Belyakov, A., Kaibyshev, R., 2016. Grain refinement kinetics and strengthening mechanisms in Cu-0.3Cr-0.5Zr alloy subjected to intense plastic deformation. Mater. Sci. Eng. A 654, 131–142. https://doi.org/10.1016/j.msea.2015.12.038

Zhu, C., Harrington, T., Gray, G.T., Vecchio, K.S., 2018. Dislocation-type evolution in quasi-statically compressed polycrystalline nickel. Acta Mater. 155, 104–116. https://doi.org/10.1016/j.actamat.2018.05.022

Zhu, Z., Shi, R., Klarner, A.D., Luo, A.A., Chen, Y., 2020. Predicting and controlling interfacial microstructure of magnesium/aluminum bimetallic structures for improved interfacial bonding. J. Magnes. Alloy. 8, 578–586. https://doi.org/10.1016/j.jma.2020.03.004